Hydride formation in open thin film metal hydrogen systems: Cahn–Hilliard-type phase-field simulations coupled to elasto-plastic deformations

Alexander Dyck [a], Johannes Gisy [a], Frederik Hille [a], Stefan Wagner [b], Astrid Pundt [b], Thomas Böhlke [a,*]

[a] Institute of Engineering Mechanics - Chair of Continuum Mechanics, Karlsruhe Institute of Technology (KIT), Kaiserstraße 10, 76131 Karlsruhe, Germany
[b] Institute for Applied Materials Materials Science and Engineering, Karlsruhe Institute of Technology (KIT), Engelbert-Arnold Straße 4, 76131 Karlsruhe, Germany

Keywords:
Open metal hydrogen system
Thin film
Hydride formation
Elasto-plastic deformations
Cahn–Hilliard-type phase-field model

A B S T R A C T

For the usage of intercalating material systems to store and convert energy of renewable sources, their phase stabilities need to be engineered to adjust to the desired operation conditions. This can, e.g., be achieved by miniaturization, leading to constraints that modify the systems thermodynamics. The experimental investigation of such systems is cumbersome, as experiments on nano-sized systems are time intensive. Numerical simulations based on chemo-mechanically coupled continuum models can serve as a tool helping to understand these systems and to study different effects of miniaturization. In this work we present a phase-field model for the example of open, constrained metal hydrogen thin film systems, that allows the prediction of the hydrogen intercalation and hydride formation. The model relies on a free energy density consisting of chemical, mechanical and interfacial parts. The first two contributions are based on measurements of the thermodynamics of open Niobium–Hydrogen thin films, that are chosen as a model. The interfacial contribution of Cahn–Hilliard-type introduces a phase-field description for both phases. To study the systems behavior a numerical implementation in the commercial Finite Element solver ABAQUS is presented. Numerical results are presented and compared to previously obtained experimental results on the open systems thermodynamics. We show, that the model is capable of reproducing experimentally observed behavior of thin films especially regarding the coexistence of α- and hydride-phase in thermodynamic equilibrium, where the equilibrium concentrations in both phases drastically differ from bulk values, and gradients in concentration and stresses result due to the interfacial constraint conditions.

1. Introduction

Intercalating systems such as metal-ion battery systems, metal hydrides or doped transition-metal oxides are often mentioned as a cornerstone in a future carbon free energy system, as they can serve as storage systems for renewable energies (Züttel et al., 2008; Armand and Tarascon, 2008; Adams and Chen, 2011; Schneemann et al., 2018; McCay and Shafiee, 2020; Xia et al., 2023), or they possess a strong potential for electronic device applications (Nichols et al., 2013; Fruchter et al., 2018; Matsumoto et al., 2020; Cichy and Świerczek, 2021). The applicability of a certain intercalating system is mainly determined by thermodynamical phase-boundaries and phase stabilities (Durbin and Malardier-Jugroot, 2013), as they define the systems' storage capacity and the temperature range of operation. In order to engineer both system properties, miniaturization is a possible pathway, as phase-boundaries and phase stabilities are strongly affected by microstructural and size effects (Schneemann et al., 2018; Wagner et al., 2019).

This mainly results from constraint conditions restricting the volumetric swelling of the host system during intercalation of another species. Commonly, intercalated atoms induce a volumetric, stress-free swelling of the lattice (Fukai, 2005). However, interfaces and constraints can suppress this expansion, especially in miniaturized systems such as thin metal films adhered to a rigid substrate (Wagner et al., 2011; Hamm et al., 2015; Burlaka et al., 2015; Spatschek et al., 2016; Burlaka et al., 2016; Wagner et al., 2019; Nichols et al., 2013), but also other materials systems with coherent interfaces (Armand and Tarascon, 2008; Di Leo et al., 2014; Phan et al., 2019). Mechanical

* Corresponding author.
E-mail address: thomas.boehlke@kit.edu (T. Böhlke).

stresses result from the constraints of these miniaturized systems, which have been shown to strongly influence solubility, stability of storage, catalytic or conductive phases, or phase transformations at all (Wagner et al., 2019; Liu et al., 2024; Fernandez et al., 2021).

Among intercalating systems, metal-hydrogen systems with a capacity to form metal-hydrides offer efficient conditions to store hydrogen produced, e.g., from water electrolysis. The hydride phase acts as the storage phase, and the storage capacity is mainly given by the width of the miscibility gap between solid solution and hydride phases (Züttel et al., 2008; Adams and Chen, 2011; Schneemann et al., 2018; McCay and Shafiee, 2020). In order to engineer solubility and hydride phase stabilities of metal hydrogen systems by constraints, thin films of Palladium–Hydrogen (Pd–H) as well as Niobium–Hydrogen (Nb–H) widely serve as model systems due to the ease of their experimental handling. Extensive studies on these systems have been performed both on films loaded by gaseous hydrogen or by means of electrochemistry, using experimental methods such as X-ray diffraction (XRD), transmission electron microscopy (TEM), scanning tunneling microscopy (STM), substrate curvature measurements or electromotoric force measurements (EMF) in the last decades, see, e.g., Zabel and Peisl (1979), Abromeit et al. (1997), Song et al. (2002), Gremaud et al. (2009), Pivak et al. (2011), Nörthemann and Pundt (2011), Baldi et al. (2014), Hamm et al. (2015), Burlaka et al. (2015), Griessen et al. (2016) and Wagner et al. (2019). Besides experimental methods, simulative approaches can lead to a better quantitative understanding of phase boundaries and phase stabilities. For both the Titanium–Hydrogen (Ti–H) as well as the Zirconium–Hydrogen (Zr–H) system, phase-field models are routinely used to predict hydride formation, growth or reorientation under applied loads on the continuum scale. For recent extensive reviews we refer to Zhu et al. (2022) for the Ti–H system as well as Jia and Han (2023) for the Zr–H system.

Phase-field models introduce a diffuse interface between phases, which allows the application of numerical methods to compute the formation of different phases, while considering mechanical stresses in a coherent system (Schwarz and Khachaturyan, 1995). The basis of a phase-field model is a free energy functional, capturing chemical contributions of the bulk material and especially it is tendency to form different phases, mechanical stresses and interface effects. The latter are introduced by considering gradients of so-called order parameters in the free energy functional (Steinbach, 2009; Steinbach and Shchyglo, 2011). A popular model relying on concentration or composition as a physical order parameter has been presented by Cahn and Hilliard (1958), who described decomposition of a two-phase system. The Cahn–Hilliard equation has been used extensively in phase-field models, see, e.g., Voskuilen and Pourpoint (2013), Bair et al. (2017), Han et al. (2019), Heo et al. (2019) and Simon et al. (2021) for applications in the Zr–H systems, as well as Armand and Tarascon (2008), Di Leo et al. (2014) and Castelli et al. (2021) and the references mentioned therein for applications in battery materials. In the context of hydrogen-based direct reduction of iron oxide, a phase-field model was proposed in Bai et al. (2022).

In the context of hydrogen storage metals, besides (Spatschek et al., 2016), to our best knowledge, no such model has been presented in order to gain a more quantitative understanding of the complex phase separation behavior of thin film metal-hydrogen systems. Thus, in this work we formulate such a phase-field model, where thin Nb–H films adhered to sapphire substrates are chosen as a model system, that offers several beneficial aspects from the experimental view point. This includes strong adhesion of the Nb film to the substrate, lattice matching between film and substrate and a small number of lattice defects such as grain boundaries (Wagner et al., 2019). These studies serve as a first approach towards understanding phase boundaries and phase interfaces in thin film systems undergoing intercalation. This treatment relies on previously obtained experimental results (Hamm et al., 2015; Burlaka et al., 2016; Wagner et al., 2019) combined with a recently proposed free energy formulation, capturing both the systems tendency to form two phases due to a long range attraction of hydrogen atoms as well as elasto-plastic deformations of Nb (Dyck et al., 2024a,b). The interface between both phases is treated as coherent and thus a barrier for phase separation exists, as predicted by Schwarz and Khachaturyan (1995, 2006).

The outline of the paper is as follows: In Section 2, experimental results on the thin film Nb–H system are summarized, which form the basis of the model presented in Section 3. Our approach towards computing the evolution of hydrides using a Finite Element scheme is summarized in Section 4 and numerical results and their comparison to experimental ones are presented in Section 5. We close our work in Section 6, including thoughts on possible extensions.

2. The thin film Nb–H system

In this section we briefly summarize experimental and model results on both bulk and thin film Nb–H systems, which have been previously published in Schober and Wenzl (1978), Nörthemann and Pundt (2008, 2011), Hamm et al. (2015), Burlaka et al. (2015, 2016), Wagner et al. (2019), Dyck et al. (2024a) and Dyck et al. (2024b). These results form the basis of our model developed in Section 3. In Nörthemann and Pundt (2008, 2011), Hamm et al. (2015), Burlaka et al. (2015, 2016) and Wagner et al. (2019), thin Nb films were produced by means of argon-ion beam sputtering on sapphire substrates, such that epitaxial Nb films with desired thickness and [110]-orientation grow on the substrates. To avoid oxidation and to facilitate hydrogen loading, the films were covered with a Pd capping layer or, if the vacuum was not broken between film preparation and hydrogen loading, with Pd islands. Hydrogen loading occurred mainly from the gaseous phase at given temperature and increasing but stepwise constant gas pressures p_{H2}. This implies, that we will focus on open systems in the following, i.e. systems with the possibility to take up hydrogen from their surrounding at a given chemical potential. To measure the films stress state and the chemical potential as a function of hydrogen concentration, hydrogen loading was performed electrochemically with defined stepwise increase of the hydrogen concentration. The latter system is, therefore, a closed system. We here assume that the stresses measured as a function of concentration for closed systems can be transferred to the open system (Wagner et al., 2019).

By means of in-situ XRD, STM, TEM, substrate curvature and EMF measurements, the thermodynamics (EMF) as well as in-plane stress states (substrate curvature), height changes (STM) and changes in crystal structure (XRD, TEM) were studied, both for open and closed systems. In open systems, upon hydrogen adsorption these experiments reveal hydride formation and coexistence of a hydrogen poor α-phase and a hydrogen rich hydride-phase at certain hydrogen pressures. In bulk Nb–H both an α'- and β-hydride-phase have been reported, with equilibrium concentrations of $c_\alpha^{\max} = 0.06\,\mathrm{H/Nb}$ and $c_\beta^{\min} = 0.72\,\mathrm{H/Nb}$ (Schober and Wenzl, 1978). In thin Nb–H films these equilibrium concentrations change due to occurring stresses resulting from constraint conditions (Wagner et al., 2019; Dyck et al., 2024a,b), and measurements hint on the hydride phase to keep the bcc structure of the matrix phase (Burlaka et al., 2017). We therefore, in this work, consider an α'-hydride phase to simplify the model. The constraint conditions of thin films, c.f. Fig. 1(a), imposed by their adherence to a substrate being much stiffer than the films, introduce large compressive stresses, c.f. Fig. 1(b). These stresses strongly alter the onset conditions of phase separation behavior and lead to drastic changes in equilibrium concentrations or even to suppression of phase transition in the case of very thin Nb–H films deforming purely elastic, c.f. Fig. 1(c).

In Dyck et al. (2024a,b) we proposed a free energy density that captures both chemical as well as mechanical contributions. They are both related to the measured EMF and the measured stress state of the film (Wagner et al., 2019). The equilibrium concentrations are $c_\alpha^{\max} \approx 0.1\,\mathrm{H/Nb}$ and $c_{\alpha'}^{\min} \approx 0.58\,\mathrm{H/Nb}$ in an elasto-plastically deforming Nb–H film at room temperature. For details we refer to Dyck et al.

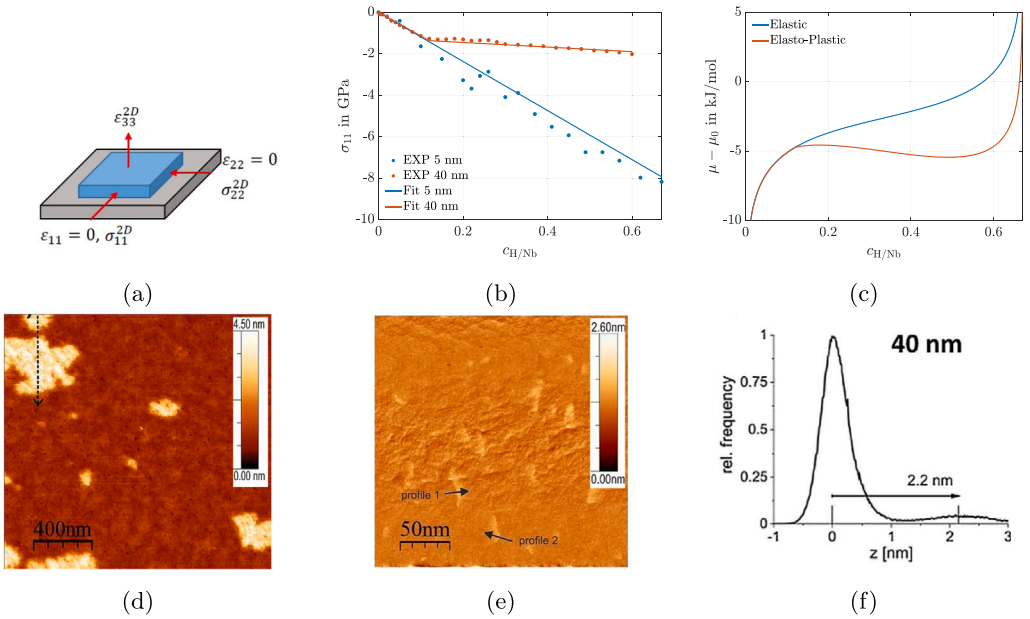

Fig. 1. (a) Constraint conditions in thin film metal hydrogen systems, imposing in-plane stresses. Reproduced with permission from Dyck et al. (2024a). (b) Occurring in-plane stresses in a 40 and 5 nm Nb film upon hydrogen absorption. The 5 nm film deforms elastically, while the 40 nm film deforms elasto-plastically. Reproduced with permission from Dyck et al. (2024a). (c) Chemical potential incorporating mechanical stresses as a function of hydrogen concentration presented in Dyck et al. (2024a), showing no phase separation in the 5 nm film and phase separation in the 40 nm film at room temperature. Reproduced with permission from Dyck et al. (2024a). (d) STM surface topography image of a 40 nm epitaxial Nb thin film adhered to sapphire substrate upon hydrogen loading at $p_{H2} = 1 \times 10^{-6}$ mbar and 293 K, showing cylindrical hydride precipitates surrounded by α-phase. Reproduced with permission from Wagner et al. (2019). (e) STM surface topography difference image of an 8 nm Niobium film after cyclic hydrogen loading at $p_{H2} = 8 \times 10^{-6}$ mbar at 293 K, showing no evidence of phase separation. Reproduced with permission from Wagner et al. (2019). (f) Relative height distributions in a 40 nm film loaded under the same conditions as in (d). Large differences in the out-of-plane expansion of α- and hydride-phase are visible. Reproduced with permission from Nörthemann and Pundt (2008).

(2024a,b). During coexistence of α- and hydride-phase, the large difference in hydrogen concentration between both phases leads to marked differences in height, which can be measured by STM (Nörthemann and Pundt, 2008, 2011). The hydride-phase expands significantly stronger than the α-phase due to the larger number of interstitial hydrogen atoms. Due to the in-plane constraint, this expansion manifests itself in an increased local height and it leads to coherency stresses at the phase interfaces, superimposed by substrate-induced stresses. These stresses affect the progression of the phase transition. The larger the concentration gradient at the interfaces, the bigger the measured height difference between the local hydride and the surrounding α-phase. As can be seen in Fig. 1(d), in a 40 nm film, the presence of cylindrical hydrides of different radii in the film is confirmed by means of this height change, c.f. also Nörthemann and Pundt (2008). Only upon further hydrogen absorption due to increased gas pressures, the precipitates can loose their cylindrical shape and become more irregular. This is accompanied by misfit dislocation formation at the phase interfaces. Thus, the interfaces can become semicoherent at later stages of hydride formation. However, the phase interfaces remain coherent for films below 39(2) nm thickness (Wagner et al., 2019). In films thinner than 8(2) nm the phase separation is found to be suppressed (Wagner et al., 2019). This could be attributed to the large substrate-induced compressive stresses. This becomes evident, when the corresponding STM measurements are studied, where no hydride-related height distribution is observed. This is evidence for a continuous transition of the α-phase into a state with a large hydrogen concentration, c.f Fig. 1(e) and Dyck et al. (2024a). Also in this state dislocation formation can happen, resulting in misfit dislocations at the film–substrate interface. Traces of such dislocations are detected by STM as surface glide steps, see the yellowish lines in Fig. 1(e).

The height difference between α- and hydride-phase in a 40 nm film becomes more evident, when the relative frequency of measured heights is studied, c.f. Fig. 1(f). We point out, that the average height change of the α-phase has been set to zero in the figure. This reveals, that on average the circular hydride precipitates that form within the α-phase expand 2.2 nm more in normal direction in the 40 nm film. This has been studied using Finite Element calculations and linked to cylindrical precipitates extending all the way from the free surface of the thin film down to the substrate interface, with an average radius of 20 – 40 nm (Nörthemann and Pundt, 2008).

The coherency of Nb film–substrate and α- and hydride-phase interfaces has been studied in detail by means of the STM measurements (Nörthemann and Pundt, 2011). It has been shown, that above a critical film thickness of 5(2) nm dislocations form at the interface between film and substrate early upon hydrogen absorption (Nörthemann and Pundt, 2011; Wagner et al., 2019). This strongly affects the resulting stress states, as misfit dislocations reduce the transmitted stresses (Rahm et al., 2022). Coherency loss at the substrate interface thus leads to reduced in-plane stresses of the films. In contrast, as indicated above the interface between the α- and the hydride-phase has been shown to stay coherent for Nb films below 39(2) nm thickness, even for large hydrogen pressures and large hydride precipitates (Nörthemann and Pundt, 2011; Wagner et al., 2019). The loss of cylindrical shape of the hydride precipitates is linked to coherency loss at the phase interfaces, which was only observed for larger film heights and long exposure to gaseous hydrogen.

3. Theory of hydride formation in the thin film Nb–H system

3.1. Basic assumptions

In order to replicate the experimentally observed hydride formation behavior we propose a thermodynamically consistent, chemo-mechanically coupled phase-field model. Our model is based on EMF and stress measurements on the thin film Nb-H system. This allows us to identify both the chemical part as well as the mechanical part of the systems thermodynamic potential. The model is related to previously published phase-field models in the context of phase separating metals, see, e.g., Anand (2012), Di Leo et al. (2014), Spatschek et al. (2016), Castelli et al. (2021), Han et al. (2019), Heo et al. (2019) and Simon

et al. (2021) and references therein. In order to arrive at a compact theory, we introduce several basic assumptions from the outset. These are discussed at the end of this section. The basic assumptions are:

- The governing equations are the mass balance of diffusing hydrogen and the balance of linear momentum. Hydrogen is assumed to occupy interstitial lattice sites in both α- and α'-phase. The hydrogen content is not conserved, as an open system exposed to gaseous hydrogen is considered, which is inspired by Di Leo and Anand (2013). Inertia effects are neglected.
- The formation of hydrogen poor α- and hydrogen rich α'- or hydride-phase is described by means of a phase-field model, relying on the concentration as a physical order parameter (Steinbach, 2009). No structural order parameter as in Guo et al. (2008), Han et al. (2019), Heo et al. (2019) and Simon et al. (2021) is introduced.
- Deformations are assumed to be small, i.e. below 10% total deformation, and the total strain $\boldsymbol{\varepsilon}$ is additively decomposed into an elastic part $\boldsymbol{\varepsilon}_\mathrm{e}$, a chemical part $\boldsymbol{\varepsilon}_\mathrm{c}$ and a plastic part $\boldsymbol{\varepsilon}_\mathrm{p}$ (Gurtin et al., 2010).
- The free energy density ψ is used as thermodynamic potential, depending on strains, hydrogen concentration, temperature and plastic variables. To introduce the phase-field, both a double well potential ψ_c, introducing the system's tendency to form α- and hydride-phase and an interfacial term ψ_i, modeling the tendency of a system to minimize the interface between different phases, are considered. This was first proposed by Cahn and Hilliard (1958) and is used in all works cited above.
- The interface between the α- and the hydride-phase is treated as coherent at all times, in agreement with the experimental observations for films below 39(2) nm thickness. Thus the lattice mismatch between α- and hydride-phase is proportional to the concentration difference between both phases. In addition, the interface between thin film and substrate is treated as staying coherently during simulations by keeping the lateral dimensions of the simulation domain constant, yielding in-plane stresses linearly increasing with hydrogen concentration. However, the experimentally informed in-plane stress state of the simulated films may be divided into two regimes with different linear stress increase as a function of hydrogen concentration, mimicking the elasto-plastic deformation of the film–substrate interface (Dyck et al., 2024a).
- The barrier for forming hydride precipitates is the coherency strain barrier introduced in Schwarz and Khachaturyan (1995) and Schwarz and Khachaturyan (2006). No further energetic barrier for precipitate formation is assumed. This implies, that as soon as the concentration limiting the stability region of the α-phase is surpassed, hydride precipitates form within the α-phase (Schwarz et al., 2020).
- Changes in temperature, e.g. due to plastic deformations, are neglected (Dyck et al., 2024a).
- The Coleman–Noll procedure (Coleman and Gurtin, 1967) is used to derive thermodynamic restrictions of the constitutive equations and resulting potential relations and a dissipation inequality. To not further increase the length of this publication, the derivation is not presented in detail. It can be found for similar models in, e.g., Gurtin et al. (2010), Anand (2012), Di Leo and Anand (2013) and Dyck et al. (2024c).
- All constitutive functions are modeled isotropically, including stiffness, hydrogen mobility and plasticity (Dyck et al., 2024a). All material parameters are assumed independent of hydrogen concentration. This implies, that changes in elastic parameters, predicted by Cahn and Larché for open systems (Larché and Cahn, 1973, 1978) and recently experimentally verified by Shi et al. (2018), are not considered. An application of the Cahn–Larché theory in the context of a phase-field model can be found in, e.g., Schwarze et al. (2017).
- Throughout this work we will call the system to be in thermodynamic equilibrium, when the chemical potential is homogeneous throughout the considered simulation domain. This implies, that in our notion, in coherent two-phase systems, a thermodynamic equilibrium is reached, as soon as the gradient of the chemical potential vanishes.
- The kinetics of the phase change are disregarded throughout this work. The main focus is on the thermodynamic driving force for hydride formation in thin film metal hydrogen systems.

3.2. Balance equations

The diffusion equation describing the diffusion of hydrogen on interstitial lattice sites within the metal is formulated for the hydrogen concentration c in moles per volume using a diffusion equation

$$\dot{c} = -\mathrm{div}\,(\boldsymbol{j})\,, \tag{1}$$

where $\boldsymbol{j}$ is the hydrogen flux. By specifying $\boldsymbol{j}$ using constitutive theory, Eq. (1) will turn out to be the Cahn–Hilliard equation (Cahn and Hilliard, 1958). A normalized concentration $c_\mathrm{H} = c/c_\mathrm{max}$ of hydrogen atoms per niobium atom H/Nb is introduced, where c_max is the maximum number of moles of hydrogen per molar volume of the host metal. The second balance equation is the balance of linear momentum

$$\mathrm{div}\,(\boldsymbol{\sigma}) = \boldsymbol{0}, \tag{2}$$

where $\boldsymbol{\sigma}$ is the symmetric Cauchy stress tensor.

3.3. Constitutive theory

A thermodynamically consistent constitutive theory is presented in the following by introducing a free energy density ψ. To this end, a set of independent variables $\Lambda = \left[\boldsymbol{\varepsilon}, \theta, c_\mathrm{H}, \underline{\alpha}\right]$ is used, where θ is the temperature and $\underline{\alpha}$ is a tuple of internal variables, later considered to be plastic strains $\boldsymbol{\varepsilon}_\mathrm{p}$ and the equivalent plastic strain ε_eq. As proposed in previous works in the context of phase-separating, elasto-plastically deforming materials, see, e.g., Anand (2012), Di Leo et al. (2014) and Castelli et al. (2021), we introduce an additive split of the free energy density into an elastic part ψ_e, a chemical part ψ_c and an interfacial part ψ_i via

$$\psi(\Lambda) = \psi_\mathrm{e}(\boldsymbol{\varepsilon}_\mathrm{e}) + \psi_\mathrm{c}(c_\mathrm{H}, \theta) + \psi_\mathrm{i}(\mathrm{grad}\,(c_\mathrm{H}))\,. \tag{3}$$

The elastic part depends on the elastic strains

$$\boldsymbol{\varepsilon}_\mathrm{e} = \boldsymbol{\varepsilon} - \boldsymbol{\varepsilon}_\mathrm{c} - \boldsymbol{\varepsilon}_\mathrm{p}, \tag{4}$$

where the volumetric chemical strains are given as

$$\boldsymbol{\varepsilon}_\mathrm{c} = \eta_\mathrm{H} c_\mathrm{H} \boldsymbol{I} \tag{5}$$

and η_H is an expansion coefficient describing the dilatation of the metal lattice due to the presence of hydrogen atoms (Wagner et al., 2019). The elastic part ψ_e is quadratic in the elastic strains

$$\psi_\mathrm{e} = \frac{1}{2}\boldsymbol{\varepsilon}_\mathrm{e} \cdot \mathbb{C}\left[\boldsymbol{\varepsilon}_\mathrm{e}\right], \tag{6}$$

where $\mathbb{C}$ is the stiffness tensor of Nb. The chemical part ψ_c is given by Dyck et al. (2024b) and Dyck et al. (2024a)

$$\psi_\mathrm{c} = \mu_0\, c_\mathrm{H}\, c_\mathrm{max} + R\theta c_\mathrm{max}\left(-r\ln\left(\frac{r}{r-c_\mathrm{H}}\right) + c_\mathrm{H}\ln\left(\frac{c_\mathrm{H}}{r-c_\mathrm{H}}\right)\right) - \frac{c_\mathrm{max}}{2} E_\mathrm{HH} c_\mathrm{H}^2. \tag{7}$$

Here μ_0 is a reference chemical potential, R is the gas constant and E_HH is a long-range attractive hydrogen–hydrogen interaction energy. It results from the interaction of dissolved hydrogen atoms via the H-induced dilatation field of the metal lattice. Hence, E_HH defines the driving force for the initiation of the phase transition in the metal hydrogen system (Wagner and Pundt, 2016), as it introduces a second well in ψ_c, indicating the systems tendency to form two phases. The

parameter r is introduced to consider electronic interactions and related second nearest neighbor blocking of H atoms on tetrahedral interstitial sites in Nb (Switendick, 1979; Wicke et al., 2005; Fukai, 2005), limiting the maximum concentration of hydrogen atoms within the lattice. Again, r can be identified by means of EMF measurements (Wagner et al., 2019). This implies, that our form of ψ_c considers both the electronic interaction of hydrogen atoms with Nb (by means of r) and the maximum number of interstitial sites available (by means of c_{max}). As in the considered Nb–H system the electronic interaction dominates at large concentrations, the parameter r determines the maximum hydrogen concentration in Nb (Dyck et al., 2024a).

Before proceeding we want to briefly comment on the specific form of ψ_c, which differs from oftentimes used approaches (Anand, 2012; Di Leo et al., 2014; Han et al., 2019; Heo et al., 2019; Simon et al., 2021). The logarithmic part is, also in our approach, based on the classic mixture entropy model for ideal gases. However, in the thin films considered in this work, not all geometrically available interstitial sites can be occupied by hydrogen atoms, due to electronic interactions between them. This implies, that the hydrogen concentration is capped at a value $c_H < 1$. In our model, this is accounted for by the introduction of the parameter r, which implies mathematically $0 \leq c_H \leq r$. The classic expression for entropy of mixing is retrieved from our formulation by setting $r = 1$. In addition, commonly, the double well form of ψ_c is introduced by considering a mixture enthalpy model, see, e.g. Gurtin et al. (2010), Anand (2012) and Spatschek et al. (2016), that introduces the systems tendency to form a second phase. In our approach E_{HH} is introduced to that end, allowing us to incorporate the mentioned EMF and stress measurements by fitting E_{HH}, and hence to couple the theory to the experiment.

The final contribution to the free energy density is the interfacial part ψ_i, which describes the systems tendency to minimize the interface between the two phases. It is given by Cahn and Hilliard (1958) and Anand (2012)

$$\psi_i = \frac{1}{2} R\theta c_{max} \lambda_c \| \mathrm{grad}\,(c_H) \|^2. \tag{8}$$

The parameter λ_c describes the width of the interface separating α- and α'-phase and $\| \mathrm{grad}\,(c_H) \|$ denotes the Frobenius norm of the concentration gradient. The chemical potential of hydrogen in Nb and the Cauchy stresses follow from potential relations via (Anand, 2012; Di Leo et al., 2014)

$$\begin{aligned} \mu &= \frac{\partial \psi}{\partial c_H} \frac{1}{c_{max}} = \frac{1}{c_{max}} \frac{\partial \psi_c}{\partial c_H} - \eta_H \nu_0 \mathrm{tr}\,(\boldsymbol{\sigma}) - \frac{1}{c_{max}} \mathrm{div} \left(\frac{\partial \psi_i}{\partial \mathrm{grad}\,(c_H)} \right) \\ &= \mu_0 + R\theta \ln \left(\frac{c_H}{r - c_H} \right) - E_{HH} c_H - \eta_H \nu_0 \mathrm{tr}\,(\boldsymbol{\sigma}) - R\theta \lambda_c \Delta c_H, \\ \boldsymbol{\sigma} &= \frac{\partial \psi}{\partial \boldsymbol{\varepsilon}} = \mathbb{C}\,[\boldsymbol{\varepsilon}_e], \end{aligned} \tag{9}$$

where $\nu_0 = 1/c_{max}$. The Laplace operator applied to the normalized concentration is Δc_H. The potential relations are assumed to hold for both elastic and elasto-plastic deformations. Having specified all equilibrium contributions, the dissipative parts, i.e. plasticity and hydrogen flux $\boldsymbol{j}$ have to be introduced. The plasticity model is a rate-independent, isotropic von Mises theory (Mises, 1928). The yield function, limiting the range of purely elastic deformations, is

$$\varphi(\boldsymbol{\sigma}', \varepsilon_{eq}) = \|\boldsymbol{\sigma}'\| - \sqrt{\frac{2}{3}} \sigma_F\,(\varepsilon_{eq}) \leq 0, \tag{10}$$

where $\sigma_F\,(\varepsilon_{eq}) = \sigma_{Y0} + h\varepsilon_{eq}$ denotes the yield stress with initial yield stress σ_{Y0} and hardening modulus h. The deviatoric part of the stress is $\boldsymbol{\sigma}'$. This captures the measured in-plane stresses shown in Fig. 1(b) as detailed in Dyck et al. (2024a). In an associated plastic flow theory, both internal variables evolve according to

$$\dot{\boldsymbol{\varepsilon}}_p = \sqrt{\frac{3}{2}} \gamma \boldsymbol{N}, \quad \dot{\varepsilon}_{eq} = \sqrt{\frac{2}{3}} \gamma, \tag{11}$$

where $\boldsymbol{N} = \boldsymbol{\sigma}'/\|\boldsymbol{\sigma}'\|$ and γ is the consistency parameter. The consistency parameter is only non-zero, when the yield condition $\varphi = 0$ and the loading condition $\boldsymbol{\sigma} \cdot \dot{\boldsymbol{\varepsilon}} > 0$ are fulfilled.

The hydrogen flux is given as Anand (2012)

$$\boldsymbol{j} = -m(c_H)\,\mathrm{grad}\,(\mu), \tag{12}$$

where $m(c_H)$ is the mobility of hydrogen in niobium. It is a function of hydrogen concentration and diffusion constant D via (Anand, 2012)

$$m(c_H) = \frac{D c_{max}}{R\theta} c_H (1 - c_H). \tag{13}$$

3.4. Closed set of governing equations

Inserting the hydrogen flux (Eq. (12)) and the potential relations (Eq. (9)) into the balance Eqs. (1) and (2) yields a set of coupled partial differential equations (PDEs), that describe diffusing hydrogen, the formation of hydrides and elasto-plastic deformations in Nb. The diffusion equation is, due to the interfacial contribution to the free energy density, a fourth-order PDE. The solution of this coupled system is detailed in the following section. The coupled system of PDEs is

$$\begin{aligned} &\mathrm{div}\,(\boldsymbol{\sigma}) = \boldsymbol{0}, \\ &c_{max} \dot{c}_H = \mathrm{div} \left(\frac{D c_{max} c_H\,(1 - c_H)}{R\theta} \mathrm{grad}\,(\mu) \right). \end{aligned} \tag{14}$$

Both boundary conditions (expressed via $\bar{(\cdot)}$) and initial conditions (expressed via $(\cdot)_0$) have to be specified for the degrees of freedom c_H and $\boldsymbol{u}$ in order to obtain a solution. Commonly, a Cahn–Hilliard equation is considered for mass conserving systems, i.e. the amount of hydrogen remains constant (Voskuilen and Pourpoint, 2013; Bair et al., 2017). However, in our work, Nb is exposed to gaseous hydrogen and diffusion into and out of the thin film can occur. This exposure is best mimicked by a boundary condition for the chemical potential of hydrogen in Nb, i.e.

$$\bar{\mu} = \bar{\mu}(p_{H2}) = \frac{1}{2} \mu_{H2}(p_{H2}) = \frac{1}{2} \left(\mu^0_{H2} + R\theta \ln \left(\frac{p_{H2}}{p_0} \right) \right), \tag{15}$$

where p_{H2} is the partial pressure of gaseous hydrogen, p_0 a reference pressure and μ^0_{H2} the reference chemical potential of hydrogen molecules, discussed in greater detail in Di Leo and Anand (2013). This will be used in the following, when hydride formation in open Nb-H-systems is investigated by means of numerical simulations.

3.5. Discussion of the model equations and assumptions

Before proceeding with details on the implementation of our model, the following remarks are in order:

- Defects of the lattice structure in a metal, e.g. grain boundaries or dislocations, can serve as potential traps for hydrogen atoms (Sofronis and McMeeking, 1989; Di Leo and Anand, 2013). These are not accounted for in our model, due to the low number of initial lattice defects in epitaxial Nb thin films (Wagner et al., 2019). In addition, hydrogen-induced vacancy formation is not considered (Čížek et al., 2004).
- The difference between occurring stresses in 5 and 40 nm films is a size effect, which results from the balance of the total elastic energy stored in a thin film and the formation energy of dislocations (Wagner and Pundt, 2016). This is not captured by our model, which is a first gradient theory, in contrast to, e.g., Forest et al. (2000). Instead we use a size dependent increased initial yield stress σ_{Y0} in order to study purely elastic behavior, c.f. Fig. 1(b).
- In the Zr–H system, commonly both a Cahn–Hilliard as well as an Allen–Cahn equation are solved, see, e.g. Voskuilen and Pourpoint (2013), Han et al. (2019), Heo et al. (2019) and Simon et al. (2021). The latter describes the evolution of structural order parameters, capturing changes in crystallographic structure or different hydride variants. As we only consider a single

hydride-phase with constant material parameters, we refrain from incorporating an Allen–Cahn equation, in order to reduce the complexity of the model.

- As stated in Section 2, the interface between thin film and substrate can become semicoherent upon hydrogen absorption by the formation of misfit dislocations. We indirectly incorporate this effect via the measured in-plane stress of the 40 nm film. This is done via the hardening modulus h as well as the yield stress σ_{Y0}, identified in Dyck et al. (2024a), resembling the experimentally observed stress release due to the coherency loss at the film–substrate interface. Still, coherency strains will occur at the substrate interface in our simulations, leading to the build up of additional in-plane stresses (Rahm et al., 2022) of a magnitude not observed in the experiments. This difference results from inhomogeneous stress relaxation occurring at the interfaces of α-phase and substrate or hydride precipitates and substrate in the experiment.
- Open systems show strongly differing hydride formation patterns compared to closed systems, as has been recently pointed out for the Pd–H system (Schwarz et al., 2020; Rahm et al., 2022; Weissmüller, 2024). We only consider open systems in our work by prescribing a chemical potential μ for hydrogen in lattice sites at the upper boundary of the simulation domain. In this setup the Nb–H α-phase transforms into the α'-hydride-phase as soon as the unstable region of the phase diagram presented in Dyck et al. (2024a) is reached. Both phases are considered to have the same lattice structure and are therefore represented by one Helmholtz free energy density curve possessing two local minima and one local maximum.
- In this work we propose to use an isotropic elastic and an isotropic, phenomenological plastic model. Both are simplifying assumptions for the considered thin film systems, as these grow epitaxially with a [110] orientation (Wagner et al., 2019). This assumption implies, that no size effects and dislocation glide on discrete slip planes at local stress concentrations are considered here. However, as this is a first effort in proposing a model for the formation of hydrides in thin film metal hydrogen systems, we stick to it and plan to extend the constitutive theory in future work using a crystal plasticity model, c.f., e.g., Wicht et al. (2020) and Prahs et al. (2023), or even discrete dislocation dynamics.

4. Numerical implementation of the theory

4.1. General approach

In the context of chemo-mechanical coupling and phase separation, partial differential equations (PDEs) of order four and their numerical solution on a domain Ω using Finite Element methods have been studied before, see, e.g., Steinbach (2009), Ammar et al. (2009), Di Leo et al. (2014) and Castelli et al. (2021) and many others. However, solving a PDE with higher order derivatives leads to difficulties, that only a limited number of element formulations fulfill, see, e.g., Wodo and Ganapathysubramanian (2011) and Zhang et al. (2013). Instead of proceeding on using non-standard Finite Element techniques, a mixed formulation can be used, which introduces an additional degree of freedom in order to split the fourth-order PDE into two second-order PDEs, doubling the number of solution variables. For examples we refer to, e.g., Ubachs et al. (2004), Di Leo et al. (2014), Forest et al. (2011), Chen et al. (2014) and Castelli et al. (2021).

However, different strategies were used. In Ubachs et al. (2004) and Di Leo et al. (2014) a micromorphic approach is used, that introduces an artificial concentration and penalizes deviations from the actual concentration. In contrast, in Chen et al. (2014) and Castelli et al. (2021) both the concentration and the chemical potential are used as numerical degrees of freedom. For the latter approach both existence and uniqueness of Finite Element solutions have been studied, see, e.g. Elliott et al. (1989), Copetti and Elliott (1992) and Barrett and Blowey (1999).

For this reason we choose a mixed formulation introducing a second chemical degree of freedom, namely the chemical potential, to numerically solve the system of coupled PDEs outlined in the previous section. We rely on the commercial Finite Element solver ABAQUS and its User Defined Element (UEL) subroutine. This allows us to use the automatic time-stepping scheme as well as the graphical user interface of ABAQUS, while offering the flexibility to define individual PDEs. To this end, each balance equation is discretized using Finite Elements and the element residuals as well as their tangents are supplied to ABAQUS. We will not go into detail with a thorough presentation of each step necessary to write a UEL, as this has been done in Chester et al. (2015). Instead we briefly present the discretization including the weak form of the PDEs. We use ABAQUS notation in all following considerations (Smith, 2009).

4.2. Mixed formulation

In order to reduce the highest derivative in the diffusion equation to two, the total hydrogen concentration c_H as well as the chemical potential μ are used as chemical degrees of freedom in our implementation. This implies, that the diffusion Eq. $(14)_2$ is replaced by two coupled PDEs, namely

$$\begin{aligned} c_{\max}\dot{c}_\mathrm{H} &= \operatorname{div}\left(\frac{D c_{\max} c_\mathrm{H}(1-c_\mathrm{H})}{R\theta}\operatorname{grad}(\mu)\right), \\ \mu &= \frac{1}{c_{\max}}\frac{\partial \psi_\mathrm{c}}{\partial c_\mathrm{H}} - \eta_\mathrm{H} v_0 \operatorname{tr}\left(\boldsymbol{\sigma}(\boldsymbol{\varepsilon}, c_\mathrm{H}, \boldsymbol{\varepsilon}_\mathrm{p})\right) - R\theta\lambda_\mathrm{c}\Delta c_\mathrm{H}. \end{aligned} \tag{16}$$

In both PDEs, the highest derivative is two. The strong form of balance equations, being solved using a Finite Element scheme is thus (c.f. Eq. $(14)_2$)

$$\begin{aligned} c_{\max}\dot{c}_\mathrm{H} &= \operatorname{div}\left(\frac{D c_{\max} c_\mathrm{H}(1-c_\mathrm{H})}{R\theta}\operatorname{grad}(\mu)\right), \\ \mu &= \frac{1}{c_{\max}}\frac{\partial \psi_\mathrm{c}}{\partial c_\mathrm{H}} - \eta_\mathrm{H} v_0 \operatorname{tr}\left(\boldsymbol{\sigma}(\boldsymbol{\varepsilon}, c_\mathrm{H}, \boldsymbol{\varepsilon}_\mathrm{p})\right) - R\theta\lambda_\mathrm{c}\Delta c_\mathrm{H}, \\ \mathbf{0} &= \operatorname{div}\left(\boldsymbol{\sigma}(\boldsymbol{\varepsilon}, c_\mathrm{H}, \boldsymbol{\varepsilon}_\mathrm{p})\right). \end{aligned} \tag{17}$$

The numerical degrees of freedom are the concentration c_H, the chemical potential μ as well as the displacement $\boldsymbol{u}$, while the plastic strains $\boldsymbol{\varepsilon}_\mathrm{p}$ and the equivalent plastic strain ε_eq are treated as internal variables, using a radial return method and an implicit Euler scheme for time integration (Simo and Hughes, 1998). We note, that using this splitting method, an open system can be studied by prescribing a boundary value for μ. All balance equations are non-dimensionalized (Castelli et al., 2021). To this end, Eq. $(17)_1$ is divided by $c_{\max}$, Eq. $(17)_2$ by $R\theta$ and Eq. $(17)_3$ by Young's modulus E. The dimensionless chemical potential is, in the following, denoted by $\hat{\mu}$.

4.3. Finite element discretization

The non-dimensionalized strong form is converted to a weak form by multiplying each PDE with a test function, integration over the computational domain Ω and an integration by parts. The test functions for each degree of freedom are w_c, w_μ and $\boldsymbol{w}_u$. The resulting weak form is

$$\begin{aligned} 0 &= -\int_\Omega \left(w_\mathrm{c}\dot{c}_\mathrm{H}\right) \mathrm{d}V - \int_\Omega \left(\frac{D c_\mathrm{H}(1-c_\mathrm{H})}{R\theta}\operatorname{grad}(w_\mathrm{c})\cdot\operatorname{grad}(\hat{\mu})\right)\mathrm{d}V, \\ 0 &= -\int_\Omega \left(w_\mu\left(\frac{1}{R\theta c_{\max}}\frac{\partial\psi_\mathrm{c}}{\partial c_\mathrm{H}} - \hat{\mu}\right)\right)\mathrm{d}V + \int_\Omega \left(\frac{v_0\eta_\mathrm{H}}{R\theta} w_\mu \operatorname{tr}(\boldsymbol{\sigma})\right)\mathrm{d}V \\ &\quad - \int_\Omega \left(\lambda_\mathrm{c}\operatorname{grad}(w_\mu)\cdot\operatorname{grad}(c_\mathrm{H})\right)\mathrm{d}V, \\ \mathbf{0} &= -\int_\Omega \left(\operatorname{grad}(\boldsymbol{w}_u)\cdot\frac{\boldsymbol{\sigma}}{E}\right)\mathrm{d}V. \end{aligned} \tag{18}$$

We use static condensation to express $\boldsymbol{\sigma}$ as a function of the nodal degrees of freedom, i.e, $\boldsymbol{u}$ and c_H. The tuple of internal variables $\underline{\alpha}$ is stored at each integration point (Simo and Hughes, 1998). The loading and consistency condition are replaced by the Karush–Kuhn–Tucker conditions (Simo and Hughes, 1998)

$$\gamma \geq 0, \quad \varphi \leq 0, \quad \gamma\varphi = 0. \tag{19}$$

The simulation time is discretized in time steps, where $t^{n+1} = t^n + \Delta t^n$ and the automatic time stepping algorithm of ABAQUS is used to specify the non-constant Δt. The time derivative in the diffusion equation is approximated by means of an implicit Euler scheme (or backward differentiation formulae of first order (Gear, 1967))

$$\dot{c}_\mathrm{H}^{n+1} = \frac{c_\mathrm{H}^{n+1} - c_\mathrm{H}^n}{\Delta t}. \tag{20}$$

Quantities from the previous converged increment are denoted by $(\cdot)^n$ in the following, while quantities from the current increment will not be marked to shorten notation. The computational domain Ω is discretized using isoparametric, hexahedral Finite Elements and linear shape functions for the continuous degrees of freedom. The solution variables as well as the test functions for all nodes in each element are collected in the vectors $\underline{c}_\mathrm{E}, \underline{w}_{\mathrm{E},c}, \underline{\hat{\mu}}_\mathrm{E}, \underline{w}_{\mathrm{E},\mu}, \underline{u}_\mathrm{E}$ and $\underline{w}_{\mathrm{E},u}$. A Galerkin ansatz is chosen, i.e. for each test function the same ansatz functions are used as for the nodal degrees of freedom. The linear ansatz functions are collected in matrices $\underline{N}_c, \underline{N}_\mu$ and $\underline{\underline{N}}_u$. This results in

$$\begin{aligned}
c_\mathrm{H}^\mathrm{h}(\boldsymbol{x},t) &= \underline{N}_c^\intercal(\boldsymbol{x})\, \underline{c}_\mathrm{E}(t), & w_\mathrm{c}^\mathrm{h}(\boldsymbol{x},t) &= \underline{N}_c^\intercal(\boldsymbol{x})\, \underline{w}_{\mathrm{E},c}(t),\\
\hat{\mu}^\mathrm{h}(\boldsymbol{x},t) &= \underline{N}_\mu^\intercal(\boldsymbol{x})\, \underline{\hat{\mu}}_\mathrm{E}(t), & w_\mu^\mathrm{h}(\boldsymbol{x},t) &= \underline{N}_\mu^\intercal(\boldsymbol{x}) \underline{w}_{\mathrm{E},\mu}(t),\\
\boldsymbol{u}^\mathrm{h}(\boldsymbol{x},t) &= \underline{\underline{N}}_u^\intercal(\boldsymbol{x})\, \underline{u}_\mathrm{E}(t), & \boldsymbol{w}_u^\mathrm{h}(\boldsymbol{x},t) &= \underline{\underline{N}}_u^\intercal(\boldsymbol{x}) \underline{w}_{\mathrm{E},u}(t).
\end{aligned} \tag{21}$$

Gradients of the degrees of freedom are expressed via B-matrices as in

$$\begin{aligned}
\mathrm{grad}(c_\mathrm{H}^\mathrm{h}(\boldsymbol{x},t)) &= \underline{B}_c^\intercal(\boldsymbol{x})\, \underline{c}_\mathrm{E}(t), & \mathrm{grad}(w_\mathrm{c}^\mathrm{h}(\boldsymbol{x},t)) &= \underline{B}_c^\intercal(\boldsymbol{x})\, \underline{w}_{\mathrm{E},c}(t),\\
\mathrm{grad}(\hat{\mu}^\mathrm{h}(\boldsymbol{x},t)) &= \underline{B}_\mu^\intercal(\boldsymbol{x})\, \underline{\hat{\mu}}_\mathrm{E}(t), & \mathrm{grad}(w_\mu^\mathrm{h}(\boldsymbol{x},t)) &= \underline{B}_\mu^\intercal(\boldsymbol{x})\, \underline{w}_{\mathrm{E},\mu}(t),\\
\mathrm{grad}(\boldsymbol{u}^\mathrm{h}(\boldsymbol{x},t)) &= \underline{\underline{B}}_u^\intercal(\boldsymbol{x})\, \underline{u}_\mathrm{E}(t), & \mathrm{grad}(\boldsymbol{w}_u^\mathrm{h}(\boldsymbol{x},t)) &= \underline{\underline{B}}_u^\intercal(\boldsymbol{x}) \underline{w}_{\mathrm{E},u}(t).
\end{aligned} \tag{22}$$

The discretized stresses and strains in each element are denoted as $\underline{\sigma}$ and $\underline{\varepsilon}$ and the trace of the stresses as $\mathrm{tr}\left(\underline{\sigma}\right) = \underline{I}^\intercal \underline{\sigma}$, where $\underline{I}$ is the identity matrix. The stiffness matrix is $\underline{\underline{C}}$. The discretized mobility, its derivative, as well as derivatives of the chemical part of the free energy density are denoted as

$$\begin{aligned}
m &= \frac{D \underline{N}_c^\intercal \underline{c}_\mathrm{E}(1 - \underline{N}_c^\intercal \underline{c}_\mathrm{E})}{R\theta},\\
m_\mathrm{c} &= \frac{D(1 - 2\underline{N}_c^\intercal \underline{c}_\mathrm{E})}{R\theta},\\
f_\mathrm{c} &= \frac{1}{R\theta c_\mathrm{max}} \left.\frac{\partial \psi_\mathrm{c}}{\partial c_\mathrm{H}}\right|_{\underline{N}_c^\intercal \underline{c}_\mathrm{E}},\\
f_\mathrm{cc} &= \frac{1}{R\theta c_\mathrm{max}} \left.\frac{\partial^2 \psi_\mathrm{c}}{\partial c_\mathrm{H}^2}\right|_{\underline{N}_c^\intercal \underline{c}_\mathrm{E}}.
\end{aligned} \tag{23}$$

Inserting the discretized degrees of freedom into Eq. (18) results in the element residuals

$$\begin{aligned}
\underline{R}_{\mathrm{E},c} &= \int_{\Omega_\mathrm{E}} \left(-\underline{N}_\mu \underline{N}_\mu^\intercal \underline{\hat{\mu}}_\mathrm{E} + \lambda_\mathrm{c} \underline{B}_c \underline{B}_c^\intercal \underline{c}_\mathrm{E} - \frac{\eta_\mathrm{H} \nu_0}{R\theta} \underline{N}_\mu \underline{I}^\intercal \underline{\sigma} + \underline{N}_\mu f_\mathrm{c} \right) \mathrm{d}V_\mathrm{E},\\
\underline{R}_{\mathrm{E},\mu} &= \int_{\Omega_\mathrm{E}} \left(\frac{\underline{N}_c \left(\underline{N}_c^\intercal \underline{c}_\mathrm{E} - \underline{N}_c^\intercal \underline{c}_\mathrm{E}^n \right)}{\Delta t} + m \underline{B}_\mu \underline{B}_\mu^\intercal \underline{\hat{\mu}}_\mathrm{E} \right) \mathrm{d}V_\mathrm{E},\\
\underline{R}_{\mathrm{E},u} &= \int_{\Omega_\mathrm{E}} \left(\underline{\underline{B}}_u \frac{\underline{\sigma}}{E} \right) \mathrm{d}V_\mathrm{E},
\end{aligned} \tag{24}$$

where we have omitted the test functions, as the residuals have to hold for all test functions. The integrals are computed using Gauß quadrature. The element residuals are evaluated for all elements and gathered in the residual vector of the system. To compute the increment $(\cdot)^{n+1}$ for each nodal degree of freedom, ABAQUS uses a Newton's method.

To compute the Newton update', derivatives of the element residuals with respect to the nodal degrees of freedom are required. These are collected in an element tangent matrix denoted as

$$\underline{\underline{K}}_\mathrm{E} = \begin{bmatrix} \underline{\underline{K}}_{\mathrm{E},uu} & \underline{\underline{K}}_{\mathrm{E},u\mu} & \underline{\underline{K}}_{\mathrm{E},uc} \\ \underline{\underline{K}}_{\mathrm{E},\mu u} & \underline{\underline{K}}_{\mathrm{E},\mu\mu} & \underline{\underline{K}}_{\mathrm{E},\mu c} \\ \underline{\underline{K}}_{\mathrm{E},cu} & \underline{\underline{K}}_{\mathrm{E},c\mu} & \underline{\underline{K}}_{\mathrm{E},cc} \end{bmatrix}. \tag{25}$$

Due to the way ABAQUS handles the Newton update (Smith, 2009; Chester et al., 2015), the residuals are multiplied by -1 before differentiation and the non-vanishing entries are given by

$$\begin{aligned}
\underline{\underline{K}}_{\mathrm{E},uu} &= \int_{\Omega_\mathrm{E}} \left(\underline{\underline{B}}_u \frac{\partial \underline{\underline{\sigma}}}{\partial \underline{\varepsilon}} \underline{\underline{B}}_u^\intercal \mathrm{d} \right) V_\mathrm{E},\\
\underline{\underline{K}}_{\mathrm{E},uc} &= \int_{\Omega_\mathrm{E}} \left(\underline{\underline{B}}_u \frac{\partial \underline{\sigma}}{\partial c_\mathrm{H}} \underline{N}_c^\intercal \mathrm{d} \right) V_\mathrm{E},\\
\underline{\underline{K}}_{\mathrm{E},\mu\mu} &= \int_{\Omega_\mathrm{E}} \left(m \underline{\underline{B}}_\mu \underline{\underline{B}}_\mu^\intercal \right) \mathrm{d}V_\mathrm{E},\\
\underline{\underline{K}}_{\mathrm{E},\mu c} &= \int_{\Omega_\mathrm{E}} \left(\frac{1}{\Delta t} \underline{N}_c \underline{N}_c^\intercal + \underline{\underline{B}}_\mu \underline{\underline{B}}_\mu^\intercal \underline{\mu}_\mathrm{E} m_\mathrm{c} \right) \mathrm{d}V_\mathrm{E},\\
\underline{\underline{K}}_{\mathrm{E},cu} &= \int_{\Omega_\mathrm{E}} \left(\frac{-\eta_\mathrm{H} \nu_0}{R\theta} \underline{N}_c \underline{I}^\intercal \frac{\partial \underline{\sigma}}{\partial \underline{\varepsilon}} \underline{\underline{B}}_u^\intercal \right) \mathrm{d}V_\mathrm{E},\\
\underline{\underline{K}}_{\mathrm{E},c\mu} &= \int_{\Omega_\mathrm{E}} \left(-\underline{N}_\mu \underline{N}_\mu^\intercal \right) \mathrm{d}V_\mathrm{E},\\
\underline{\underline{K}}_{\mathrm{E},cc} &= \int_{\Omega_\mathrm{E}} \left(\underline{N}_c \underline{N}_c^\intercal f_\mathrm{cc} + \lambda_\mathrm{c} \underline{B}_c \underline{B}_c^\intercal - \frac{\eta_\mathrm{H} \nu_0}{R\theta} \underline{N}_c \underline{I}^\intercal \frac{\partial \underline{\sigma}}{\partial c_\mathrm{H}} \underline{N}_c^\intercal \right) \mathrm{d}V_\mathrm{E}.
\end{aligned} \tag{26}$$

The algorithmic tangent for an isotropic von Mises elasto-plastic material, i.e. $\partial \underline{\sigma} / \partial \underline{\varepsilon}$, has been summarized and discussed in detail in Simo and Hughes (1998) and is not repeated here. The change in stress due to a variation in hydrogen concentration is $\partial \underline{\sigma} / \partial c_\mathrm{H} = -\eta_\mathrm{H} \underline{\underline{C}}\, \underline{I}$.

5. Hydride formation in the thin film Nb–H system

5.1. Simulation model

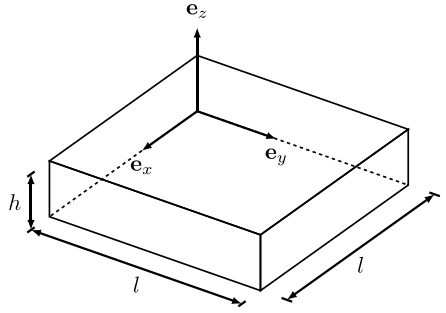

Fig. 2. Schematic of the thin film geometry and the used coordinate system.

The thin Nb film adhered to a rigid substrate and exposed to gaseous hydrogen at its top is modeled as a cuboid, c.f. Fig. 2 and Table 1 for the dimensions l and h. The domain is discretized by hexahedral elements with an edge length of 2.5 nm. A resolution study using 1.5 and 2 nm edge length has revealed no deviation in the fields of interest, indicating a sufficient resolution. The adherence of the thin film to the substrate is introduced by means of a clamped condition at the bottom. As stated in Section 3 this will lead to in-plane stresses, differing in magnitude from the semicoherent films studied in experiments. In order to approximate the large in-plane extension in comparison to the height of the thin film, i.e. $h \ll l$, Periodic Boundary Conditions (PBCs) are used on the sides of the domain for $\underline{c}_\mathrm{E}$ and $\underline{\hat{\mu}}_\mathrm{E}$, while $\underline{u}_\mathrm{E}$ is restricted by symmetry conditions. On top, mimicking the exposure to an atmosphere with gaseous hydrogen, i.e. an open system, a chemical potential is prescribed, c.f. Eq. (15).

For all simulations conducted, the concentration is prescribed homogeneous initially and the corresponding strains, chemical potential,

Table 1
Geometrical, mechanical and chemical parameters.

Symbol	Value	Source	Symbol	Value	Source
l	200 nm	This work	h	40 nm	Dyck et al. (2024a)
E	132 GPa	Dyck et al. (2024a)	ν	0.3	Dyck et al. (2024a)
σ_Y	1365 MPa	Dyck et al. (2024a)	γ	10.7 GPa	Dyck et al. (2024a)
R	8.314 J/mol/K	Dyck et al. (2024a)	θ	300 K	Dyck et al. (2024a)
$v_0 = 1/c_{max}$	9.713×10^3 mm^3/mol	Dyck et al. (2024a)	μ_0	−15.2 kJ/mol	Dyck et al. (2024a)
η	0.058	Dyck et al. (2024a)	E_{HH}	20.2 kJ/mol	Dyck et al. (2024a)
λ_c	1×10^{-5} mm	This work	r	0.67	Dyck et al. (2024a)

internal variables and stresses are computed in an initial step. All geometric and material parameters describing both the mechanical as well as the chemical properties are summarized in Table 1, where most material parameters are taken from Dyck et al. (2024a). As stated in Section 3, both E_{HH} and r result from EMF and stress measurements. Parameters not used in Dyck et al. (2024a) are the diffusion constant D and the interfacial parameter λ_c. The diffusion constant is chosen arbitrarily, as the main concern of this work is the study of an equilibrium between α- and hydride-phase. As the equilibrium state will be identical, irrespective of the chosen diffusion constant, this is suitable (Di Leo et al., 2014; Miehe et al., 2014). The interface parameter λ_c, specifying the width of the phase-separating interface, is chosen such that the used element size of 2.5 nm is at least five times smaller than the interface width, c.f. Cahn and Hilliard (1958), Di Leo et al. (2014) and Castelli et al. (2021) for details. We want to point out, that smaller values of the chosen interface parameter would not result in differing hydride precipitate shapes, size or concentration distribution within them (Miehe et al., 2014). The chosen value leads to faster convergence in the conducted Finite-Element simulations.

5.2. Homogeneous boundary conditions

We start by investigating model predictions for a homogeneous boundary chemical potential $\bar{\mu}$, resembling an open system exposed to gaseous hydrogen with constant and homogeneous partial pressure p_{H2} at the top surface of the film. We compare simulation results to analytic considerations of elasto-plastically deforming Nb-H-systems presented in a previous publication (Dyck et al., 2024a).

In an adhered thin film loaded with hydrogen, the in-plane stress state can be computed analytically as a function of c_H for elastic and elasto-plastic deformations, as long as the concentration is homogeneous. Thus the chemical potential given in Eq. (9), neglecting the interfacial contribution, can be investigated as a function of c_H, shown in Fig. 3. For an elastic film no phase separation is present at room temperature, as the large compressive stresses suppress hydride formation and μ is monotonically increasing in c_H (Dyck et al., 2024a). However, in the elasto-plastic case, the chemical potential is non-monotonic due to the lower stresses. As soon as the coherency strain energy barrier (Schwarz and Khachaturyan, 1995, 2006) is surpassed, i.e. $c_H > c_\alpha^{sp} \approx 0.17$ H/Nb (Dyck et al., 2024a), the system will transform into the hydride-phase and take up hydrogen until it has fully transformed. The critical concentration c_α^{sp} is defined by the local maximum of the chemical potential of the homogeneously treated material (Dyck et al., 2024a). This is equal to the spinodal concentration in spinodally decomposing systems, and hence we use the same suffix sp to denote the critical concentration of the α-phase as c_α^{sp}. As soon as $c_H > c_\alpha^{sp}$ the film takes up hydrogen until hydride has formed everywhere, which results in a flat plateau in the μ, c_H-diagram. Both an elastically deforming as well as an elasto-plastically deforming film are simulated using the model and implementation outlined in this work. The initial concentration is chosen to be 0.05 H/Nb at $t = t_0$, as the focus is on the onset of hydride formation. Subsequently, the boundary chemical potential is increased stepwise, mimicking a stepwise increase in p_{H2}, and held constant until an equilibrium between hydrogen in the thin film and the gaseous hydrogen has been reached, i.e. μ is homogeneous in the entire film. For this, the boundary condition is prescribed homogeneously on all nodes on top of the simulation domain. The boundary chemical potential is held constant, until the system is in thermodynamic equilibrium. This happens, as soon as the concentration is homogeneous throughout the film. Upon an increase in chemical potential, the concentration increases at the top of the thin film and hydrogen diffuses towards the film–substrate interface until the chemical potential (and c_H) are homogeneous. As soon as the coherency strain energy barrier is surpassed, the hydride-phase forms homogeneously at the top of the film and grows all the way to the bottom, as outlined below.

Results of Finite-Element simulations are shown in Fig. 3 in comparison with model predictions, where the numerical results are shown as black dots and dashed lines. Equilibrium configurations, i.e. simulation results with a homogeneous chemical potential and a homogeneous hydrogen concentration in the entire film, are denoted by dots. These are connected through non-equilibrium states indicated by dashed lines. Some important time steps in the simulation for $t > t_0$ are marked separately as discussed below for both the elastic and the elasto-plastic films. Until the onset of plastic deformation, both models result in the same μ, c_H-curve. Only after the onset of plastic deformation at $t = t_7$, where the concentration induced stresses surpass the yield limit, the curves separate.

The elastically deforming film does not show phase separation. This was shown, e.g., experimentally in Hamm et al. (2015) and based on modeling in Dyck et al. (2024a). This implies, that dislocation formation and stress relaxation are a prerequisite for hydride formation in thin film Nb–H systems. Instead the α-phase takes up large amounts of hydrogen without forming the hydride, even for large hydrogen pressures, c.f. the time steps t_{10} and following denoted in blue in Fig. 3(a). In order to increase the absorbed amount of interstitial hydrogen within the α-phase, a large increase in the partial pressure of gaseous hydrogen is necessary, c.f. the increase in the boundary value from t_7 to t_{25} (blue). As a final remark concerning the purely elastic situation we want to point out, that the Finite Element result is identical to the analytical model prediction.

In contrast, the elasto-plastically deforming film forms a hydride-phase as soon as the increasing hydrogen gas pressure leads to a concentration $c_H > c_\alpha^{sp}$ at $t > t_{13}$. This will happen at the film surface first, since the increasing chemical potential is applied at the surface in the model. Hence, the film transforms into the hydride-phase at the entire top surface, due to the chosen homogeneous boundary condition. However, during $t_{13} < t < t_{14}$ the film is not in thermodynamic equilibrium and the hydride continues to grow all the way down to the substrate, where growth occurs solely in $\boldsymbol{e}_z$ direction. Thus the thin film takes up hydrogen at a constant chemical potential until it is fully transformed into the hydride phase, which can be seen by the horizontal dashed line in Fig. 3 connecting t_{13} and t_{14} (orange). This is a direct consequence of the elastic energy barrier resulting from the coherent phase interfaces according to the theory of Schwarz and Khachaturyan (1995) and Schwarz et al. (2020). We once again want to point out, that the initial yield stress as well as the hardening modulus identified in Dyck et al. (2024a) incorporate implicitly the coherency loss at the film substrate interface. Once the entire film has transformed, the chemical potential μ resulting from the Finite Element simulation again follows the analytic model of Dyck et al. (2024a), c.f. the time steps in orange in Fig. 3(a). To more clearly outline the hydride

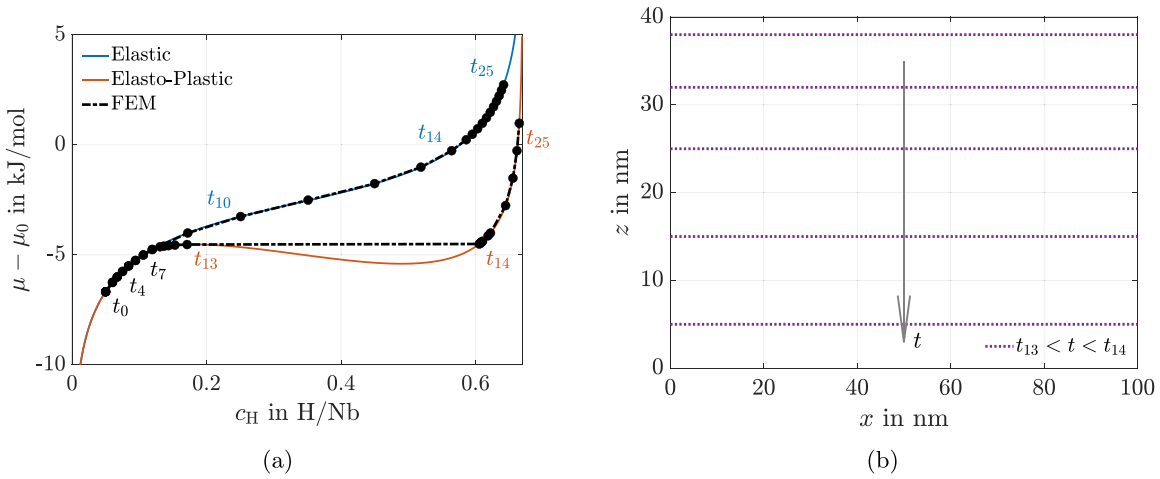

Fig. 3. (a) Evolution of the total hydrogen concentration for a stepwise increasing homogeneous chemical potential. Both a linear elastic and an elasto-plastic material behavior are studied. The results of an analytic consideration presented in Dyck et al. (2024a) are shown in color, while the numerical results are shown in black. The dots mark time steps with prescribed chemical potential at equilibrium, while the dotted lines are the non-equilibrium states. Some simulation times are marked with the respective step number as discussed in the text. (b) Propagation of the phase boundary between the α- and hydride-phase for $t_{13} < t < t_{14}$. The hydride-phase grows in e_z-direction starting at the top. All lines shown are non-equilibrium states. As soon as $t \geq t_{14}$ the entire system has formed the hydride.

formation, Fig. 3(b) shows non-equilibrium time steps of the phase boundary between the hydride- and α-phase in the range $t_{13} < t < t_{14}$. As the formation of hydride is initiated on the entire top surface, the only growth mode is in e_z-direction. With increasing time, the phase boundary grows towards the substrate interface, while the thin film takes up hydrogen at the given constant boundary chemical potential, i.e. a constant hydrogen gas pressure p_{H2}. At $t = t_{14}$ the system is in equilibrium, i.e. the chemical potential is homogeneous, and has formed hydride entirely.

5.3. *Fluctuating boundary conditions*

We now impose a fluctuating boundary condition $\bar{\mu}$, i.e. an artificially fluctuating hydrogen gas pressure p_{H2} (c.f. Eq. (15)) on the top of the thin film, in order to study equilibrium concentrations, stress states, height changes of the thin film and hydride geometries during coexistence of α- and hydride-phase, observed in experiments (Burlaka et al., 2017, 2016; Wagner et al., 2019). In order to do this, a homogeneous initial concentration of 0.13 H/Nb is applied. As this simulation is computationally more demanding and the initial steps are identical to the results shown above, this larger concentration value is chosen. Again, by prescribing a boundary value of the chemical potential we initiate hydride formation. Instead of prescribing a homogeneous boundary condition as in the discussion before, we use a locally fluctuating value. This only locally leads to concentrations surpassing the coherency strain energy barrier, while at other positions in the simulation domain this energy barrier is not surpassed. Thus, hydride precipitates form locally within the α-phase and their nucleation and growth is subsequently studied. To this end, the fluctuating boundary value is chosen in $\bar{\mu} \in [-5.1, -3.9]$ kJ/mol and applied during $t_0 < t \leq t_1$. As soon as locally a hydride precipitate forms in the simulation domain, $\bar{\mu} = -4.9$ kJ/mol is applied and held constant, until an equilibrium is reached in the entire film at $t = t_2$. Subsequently, $\bar{\mu}$ is increased stepwise by 0.1 kJ/mol during $t \in [t_3, t_4, t_5, t_6]$ and the growth of the precipitate as well as equilibrium concentrations are investigated further. All equilibrium states are depicted in Fig. 4(a) and connected by a dashed line, denoting the non-equilibrium states. In Fig. 4(b), the volume averaged concentration $\langle c_H \rangle$ in H/Nb is shown during this simulation, while in Fig. 4(c)–(f) the resulting concentration field is shown for several time steps. In the equilibrium state at $t = t_2$, part of the thin film has transformed to the hydride-phase, c.f. Fig. 4(d). Subsequent increases in $\bar{\mu}$ lead to an uptake of hydrogen, a growth of the precipitate and equilibrium states at $t = t_3$ and $t = t_4$, where both phases coexist, because the energy barrier has not yet been overcome in the entire film, see also Fig. 4(e) and (f). Accordingly, a subsequent increase in $\bar{\mu}$ from t_4 to t_5 leads to hydride phase formation in the entire film, visible by the sharp increase in $\langle c_H \rangle$ during $t_4 < t \leq t_5$ shown in Fig. 4(b). After the entire film has formed hydride, i.e. for $t > t_5$, a small increase in $\bar{\mu}$ leads only to a slight increase in $\langle c_H \rangle$, as expected when considering the analytic model (Dyck et al., 2024a). Again, as in the discussion above, the Finite Element results are in good agreement with the analytical model prediction. A slight deviation is due to heterogeneous stress and plastic strain distribution, which will be discussed in Fig. 5(b)–(d).

In order to reveal the effects of interface stresses and plastic strains on the phase transformation we proceed by studying the coexistence state of α- and hydride-phase in the model with fluctuating chemical potential in more detail, c.f. Fig. 5(a)–(d). Shown are the concentration c_H, normal stress components σ_{11} and σ_{33} in addition to the equivalent plastic strain ε_{eq} along a vertical path, i.e. along the e_z-axis, for the equilibrium states t_2, t_3, t_4 and t_5. The in-plane stress σ_{22} is not shown, as it is, due to the isotropic stiffness tensor, identical to σ_{11}. In addition, black dotted lines are shown, in order to indicate the interface of α- and hydride-phase to analyze the stress states depicted in Fig. 5(b)–(c). The interface position is determined by averaging the maximum and minimum concentration along the path and choosing the z-coordinate, where c_H exceeds this value. For t_2 and t_3 the interface position coincides.

Notably, during the transformation stages, where α- and hydride-phase coexist, the equilibrium concentrations in both phases differ from their theoretical values predicted in Dyck et al. (2024a), c.f. Fig. 5(a). This results from the strongly heterogeneous stress state and corresponding stress gradients, c.f. Fig. 5(b)–(c), when crossing the phase interface in the coexistence of α- and hydride-phase. Within the α-phase, i.e. close to the film–substrate interface below the hydride growing from the top, the in-plane stresses σ_{11} and σ_{22} are homogeneous and the out-of-plane stresses σ_{33} vanish, as is to be expected for a single phase field in a 2D constrained system. However, in the vicinity of the phase interface this drastically changes. As there is a large concentration step between the hydride-phase and the α-phase and the phase interface is coherent, the stresses increase gradually and significantly in magnitude when crossing the phase-interface. This is due to the fact, that the hydride cannot expand in-plane, as it is surrounded by α-phase, c.f. Fig. 6(b), and its out-of-plane expansion is hindered as well by the adjacent α-phase, yielding additional in-plane stress contributions due to Poisson's effect. Hence, increasingly compressive

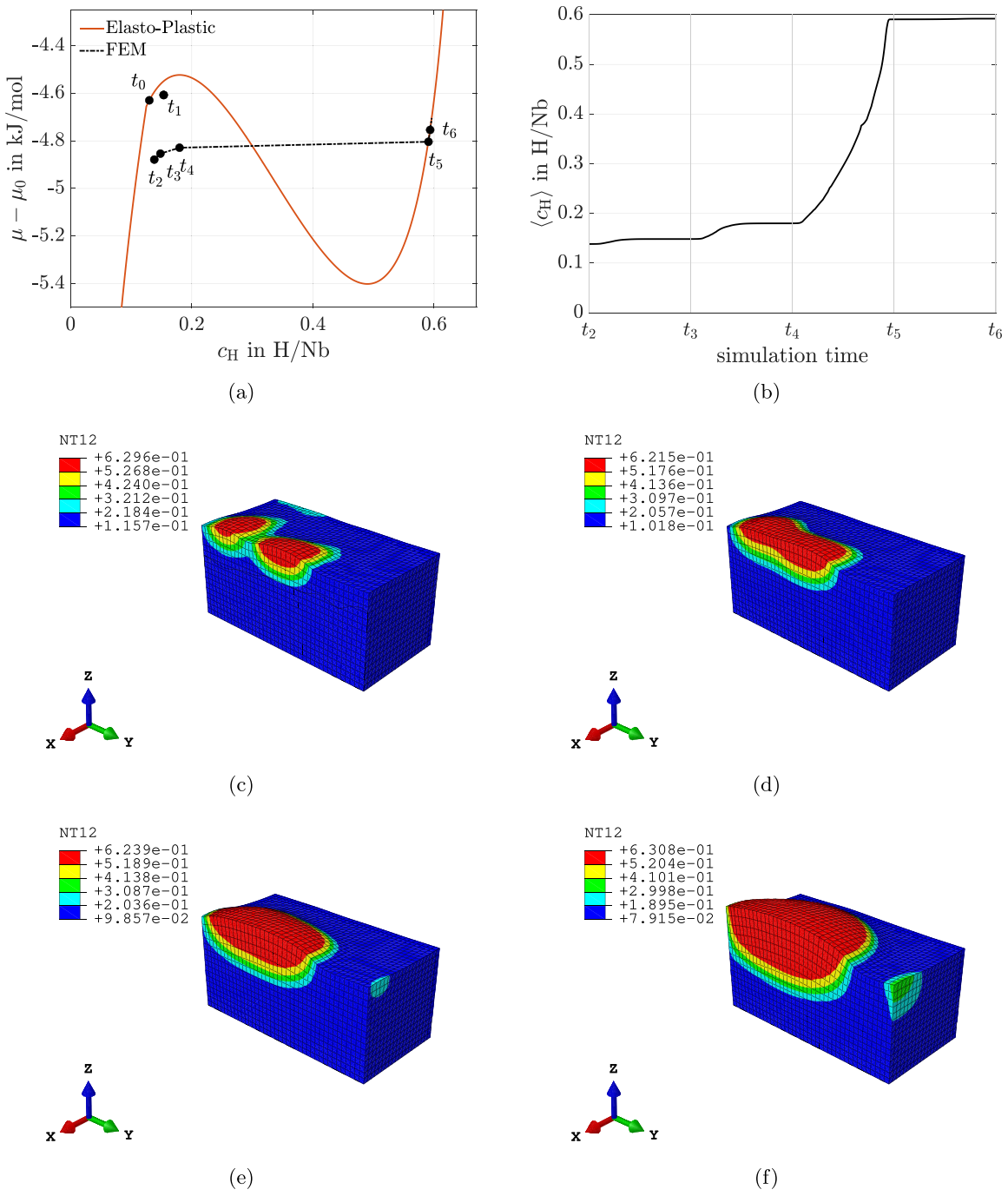

Fig. 4. (a) $\mu(c_H)$ predicted by the analytical model of Dyck et al. (2024a) is shown in orange. Finite Element results averaged over the simulation domain are shown in black. At $t = t_0$ the simulation is initiated in a homogeneous state. A fluctuating $\tilde{\mu}$ is applied on top of the film and held until, at $t = t_1$, hydride has formed. Subsequently $\tilde{\mu}$ is applied homogeneous until an equilibrium is reached at $t = t_2$. From then on, $\tilde{\mu}$ is increased stepwise for $t > t_2$ and the resulting equilibrium states are depicted by dots. (b) The volume averaged hydrogen concentration $\langle c_H \rangle$ in the film for increasing time. (c)–(f) Simulation results for the concentration c_H at several time steps. A cut through the simulation domain at $x = 50\,\text{nm}$ in the $\boldsymbol{e}_y$-$\boldsymbol{e}_z$-plane is depicted. The displacement due to the chemically induced lattice dilatation is amplified ten times. (c) c_H at $t = t_1$. (d) c_H at $t = t_2$. (e) c_H at $t = t_3$. (f) c_H at $t = t_4$.

in-plane stresses result when crossing the phase interface in direction from the α-phase to the hydride-phase. Only at the free boundary, i.e. close to $z = 40\,\text{nm}$, the hydride expands not only vertically but also in-plane, as it is not surrounded by α-phase. This leads to decreasing in-plane stresses σ_{11} and σ_{22} at the top of the film. Consequently, the out-of-plane stresses σ_{33} are also markedly heterogeneous in the vicinity of the phase interface. At the stress free top of the thin film they vanish, while they vary significantly when crossing the phase interface.

In vertical direction the hydride-phase imposes tensile stress in the α-phase, while the α-phase imposes compressive stress in the hydride due to the different local hydrogen concentrations and the resulting different lattice expansions. Remarkably, the stress gradients resulting at the phase interfaces in Fig. 5(b)–(c) impose a feedback-loop to the local hydrogen concentrations in the vicinity of the phase interface, where the local hydrogen concentrations differ from the equilibrium concentrations within the phases. Hence, coupled stress and concentration gradients result at the phase interfaces, leading to the minimization of the total strain energy of the system. According to Fig. 5(a), the concentration gradients extend up to 5 nm in both directions in the vicinity of the phase interface, with increased concentration in the

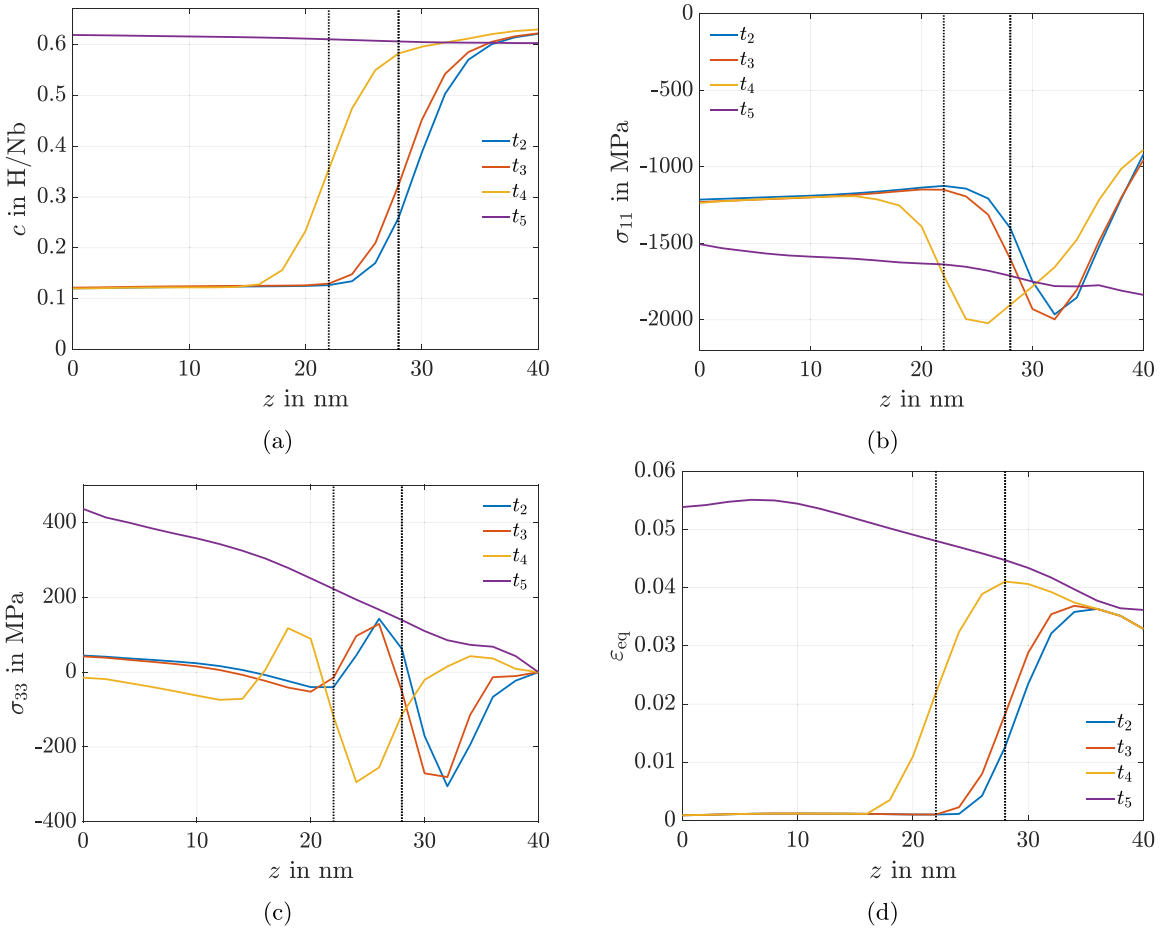

Fig. 5. Concentration, stress profiles and equivalent plastic strain along a path in e_z direction. The simulation time increases from t_2 to t_5. The phase boundary between hydride and α-phase is indicated by the dotted black line. (a) Concentration along the path. (b) In-plane stress component σ_{11} along the path. σ_{22} is similar due to the assumed isotropic stiffness tensor. (c) Out-of-plane stress component σ_{33} along the path. (d) Equivalent plastic strain ε_{eq} along the path.

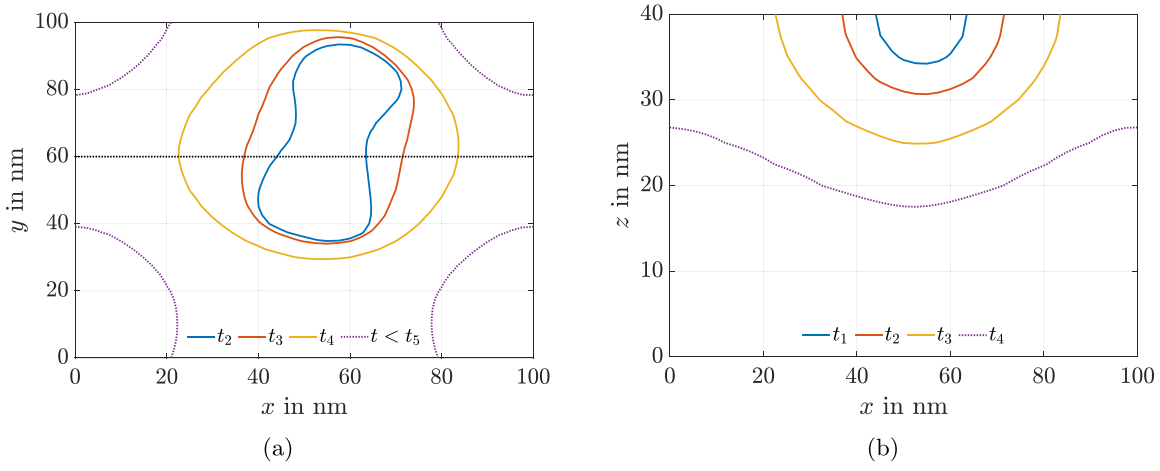

Fig. 6. Concentration isolines $c_H = 0.5$ H/Nb in equilibrium states $t \in [t_2, t_3, t_4]$. In addition, a non-equilibrium state $t_4 < t < t_5$ is shown dotted. (a) View from top. A dotted black line is included to show the position of a vertical cut at $y = 60$ nm through the film, shown in (b).

α-phase and depleted hydrogen concentration in the hydride-phase. We note, that this value of 5 nm is also a result of the choice of $\lambda_c = 1 \times 10^{-5}$ mm.

The evolution of these heterogeneous stress and concentration fields can be easily followed by comparing the numerical results of t_2, t_3 and t_4, which all show qualitatively similar behavior but at different positions in the film height, due to the moving interface, see Fig. 5(a)–(d). At $t = t_5$ the entire film has transformed into the hydride-phase and the phase interface has vanished. As mentioned above, the resulting concentrations and stresses are still not fully homogeneous, due to the heterogeneity in the equivalent plastic strains ε_{eq} in previous simulation steps, c.f. Fig. 5(d). This heterogeneity arises due to the heterogeneous hydrogen concentration and the interface between the

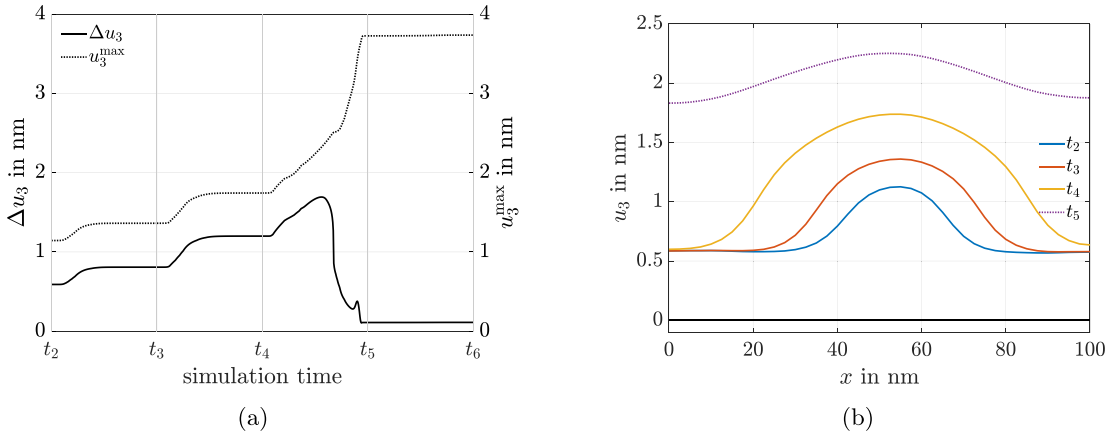

Fig. 7. (a) Maximum displacement (dotted line, right axis) $u_3^{\max}$ in $\boldsymbol{e}_z$-direction and difference between maximum and minimum displacement (solid line, left axis) Δu_3 on the top of the model at $z = z_{\max}$ as a function of time. (b) Displacement u_3 in $\boldsymbol{e}_z$-direction along a path on top of the thin film for four time steps. The simulation time increases from t_2 to t_5. In black the displacement without hydrogen loading is shown.

α- and the hydride-phase. It explains, why the results averaged for the entire film do not match the analytic predictions discussed in Fig. 4(a). Ultimately this heterogeneous distribution is a result of the fluctuating chemical potential applied on top of the simulation domain. A final remark for these results concerns the tensile stress σ_{33} at $z = 0\,\text{nm}$ for $t = t_5$, c.f. Fig. 5(c). This results from the heterogeneous distribution of plastic strains within the thin film, c.f. Fig. 5(d), and does not occur in the simulations presented in Fig. 3, where all fields are homogeneous. This tensile out-of-plane stress is only one-third of the in-plane stresses, but clearly affects the equilibrium concentration in the hydride-phase, which is larger at the bottom, c.f. Fig. 5(a).

We now proceed by studying the geometries of hydride precipitates surrounded by α-phase and their growth due to increasing p_{H2}. Results in the form of concentration isolines $c_{\text{H}} = 0.5\,\text{H/Nb}$ are depicted in Fig. 6 when viewed from above (a) and for a vertical cut (b). The resulting surface displacement of the film in $\boldsymbol{e}_z$-direction is shown in Fig. 7(b). In Fig. 6 the y-position for the vertical cut is indicated in (a) by a dotted black line. Again, the equilibrium states t_2, t_3 and t_4 are shown. In addition, the dotted violet line shows a non-equilibrium state $t_4 < t < t_5$. This allows us to discuss the evolution of the precipitate geometry before the entire film has transformed into the hydride-phase.

Initially, at $t = t_2$, a non-circular hydride precipitate has formed close to the film surface, emerging from two adjacent circular hydride nuclei. With increasing p_{H2} this irregular shape grows and becomes circular at t_3 and t_4. In our interpretation this is due to the in-plane stress state, that favors circular precipitate shapes. The hydride geometry shown in Fig. 6(a) for $t \in [t_2, t_3, t_4]$ closely resemble the experimentally determined geometries depicted in Fig. 1(b) with radii up to 40 nm. Both small regions with irregular shapes, as well as larger regions with circular shapes have been reported to form in the same film (Burlaka et al., 2016). As the simulation domain is limited in space for computational reasons, we do not see these shapes at the same equilibrium steps, but throughout several equilibrium steps. The experimentally determined range of radii of the precipitates resembles the radius of the precipitate shown in Fig. 6(a) and it is evolution with p_{H2}. However, in contrast to results presented in Nörthemann and Pundt (2008), the precipitates do not grow straight to the bottom of the film–substrate interface in a cylindrical shape. Instead, before the hydride-phase grows all the way to the substrate in our simulations, the entire surface of the film has transformed to the hydride-phase. This is indicated by the non-equilibrium state shown as dotted line in both Fig. 6(a) and (b). In our interpretation, this deviation of the simulation results and the experimental observations results from the coherent film–substrate interface in our simulations. Even though, as mentioned above, the plasticity parameters are determined by means of a semicoherent film–substrate interface, the coherency in our simulations introduces additional compressive in-plane stresses at the film–substrate interface, which prevent the growth of the precipitates towards the substrate, before the entire top of the simulated film has formed the hydride-phase.

Finally, in Fig. 7, we compare the simulated changes in height to experimentally determined values shown in Fig. 1(f). Both the maximum displacement $u_3^{\max}$ in $\boldsymbol{e}_z$-direction of the top (dotted line, right axis), as well as the difference $\Delta u_3 = u_3^{\max} - u_3^{\min}$ between the maximum and minimum displacement (solid line, left axis) are shown in Fig. 7(a). To make this difference Δu_3 more clear, the u_3 displacement in $\boldsymbol{e}_z$-direction is depicted in Fig. 7(b) for $t \in [t_2, t_3, t_4, t_5]$. With time, the maximum displacement increases, especially when the entire film forms hydride in the range $t_4 < t < t_5$, in close analogy to the uptake of hydrogen shown in Fig. 4(b). The maximum displacement $u_3^{\max}$ observed in our simulation is slightly below the maximum observed in the experiments, which is at 4.6 nm, c.f. Nörthemann and Pundt (2008). As dislocation steps and semicoherent interfaces were both not explicitly considered in our model but observed in Nörthemann and Pundt (2008), this model prediction is in pretty good agreement to the experimental results. Concerning Δu_3, i.e. the difference in u_3 displacement between α- and hydride-phase, the simulated results are in a similar range as the observed ones. The growth of the precipitates discussed above proceeds first in-plane and only later down to the substrate interface, thus the difference in height between α- and hydride-phase is not as pronounced as in the experiments, where, on average, a difference of 2.2 nm was observed, c.f. Fig. 1(f). This is in agreement with the considerations presented in Nörthemann and Pundt (2008), where it was shown, that only cylindrical precipitates can reproduce the experimentally observed height differences. However, as we do not incorporate stress relaxation at the interface between substrate and Nb film, these cannot be reproduced by our phase-field model.

6. Summary and conclusion

In the present work, a chemo-mechanically coupled phase-field model is presented, in order to study phase transformation in hydride forming thin-film open metal hydrogen systems. The open Nb–H system is utilized as a model, due to the abundance of experimental data available. The model combines a Cahn–Hilliard-type diffusion equation and the balance of linear momentum in a small strain setting and includes both chemical and plastic deformations. The free energy density is chosen as the thermodynamic potential and additively decomposed into a chemical part, introducing the tendency of the metal hydrogen system to form α- and hydride-phases, an elastic part, introducing deformations of Nb, and an interfacial contribution introducing the systems tendency to minimize interfaces between both phases. The chemical and the

elastic part are informed by experiments. The implementation of the model using a splitting method and the commercial Finite Element solver ABAQUS is presented. Within the model framework, the α-phase transforms locally into the hydride-phase as soon as the coherency strain energy barrier, computed analytically in a previous publication, c.f. Fig. 3, is surpassed due to increasing hydrogen concentration. As open systems are considered, the hydrogen gas pressure is directly prescribed as a boundary condition on the simulation domain. Numerical simulations are conducted using both a homogeneous as well as a fluctuating boundary condition. The former allows us to verify the simulation results against analytic predictions, while the latter gives insight into the coexistence of hydride- and α-phase.

The main results are summarized as follows:

- The numerical simulations confirm the absence of hydride formation for purely elastic Nb–H thin films.
- The numerical simulations reproduce analytical considerations regarding the coherency strain energy barrier of elasto-plastic Nb–H films and the resulting critical concentration of the α–phase during hydrogen loading with a homogeneous boundary condition, c.f. Fig. 3. In accordance with the theory of open coherent systems, in the model with homogeneous surface chemical potential the film entirely transforms into the hydride phase, once the elastic energy barrier is surpassed.
- The model with locally fluctuating surface chemical potential can be used to investigate coexistence states of α- and hydride-phase in open systems at a thermodynamic equilibrium, i.e. at a homogeneous chemical potential below the global elastic barrier at which the entire film transforms into the hydride-phase. Coupled stress and concentration gradients result at phase interfaces. Hence, the local concentrations at phase interfaces differ significantly from analytical predictions (Dyck et al., 2024a), where no interface between α- and hydride-phase was considered, with increased concentration in the α-phase and reduced hydrogen concentration in the hydride-phase. The gradients extend 5 nm into the single phase fields for the chosen simulation domain and parameters.
- The geometries of hydride precipitates at the surface of the film match experimental results of STM measurements on open systems, c.f. Fig. 6. However, the cylindrical growth mode of the precipitates from the film surface towards the substrate concluded in Nörthemann and Pundt (2008) is not reproduced by the model predictions. Supposedly this is due to the assumed coherency of the film–substrate interface in our simulations, which differs from the experimentally observed relaxed interface of hydride-phase and substrate in the investigated Nb–H thin films.
- The height changes during hydrogen loading measured on open systems using STM are reproduced fairly well, even though the hydride growth modes in the simulation and in the experiments differ due to the different coherency states of the film–substrate interface. However, again, due to the assumed coherency of the interface, numerical values are about 0.4 nm smaller compared to the experimental values, as the simulated precipitates do not grow all the way to the substrate.
- The results gained for the model system of adhered Nb–H thin films in the present work can be transferred to the thermodynamics of other intercalating systems with constraint conditions.

In future work, we plan to include several of the outlined aspects differing from the experimental conditions to the model, by relaxing some of the assumptions introduced in this work. These include:

- As the thin films observed in experiments are either epitaxial or nanocrystalline (Wagner et al., 2019), both the isotropic elasticity as well as the isotropic, phenomenological plasticity model could be replaced by a mechanism based model, such as crystal plasticity (Prahs et al., 2023).
- Finally, the proposed model can be used to study hydride dissolution during hydrogen release, in addition to the well known hysteresis effect (Schwarz and Khachaturyan, 1995), which has not been done in this work.

In addition the authors plan to investigate hydride precipitate shapes and sizes quantitatively using the model, in order to identify the key influencing factors for hydride formation during hydrogen absorption.

CRediT authorship contribution statement

Alexander Dyck: Writing – original draft, Visualization, Software, Methodology, Investigation, Formal analysis, Conceptualization. **Johannes Gisy:** Writing – review & editing, Software, Formal analysis. **Frederik Hille:** Writing – review & editing, Software, Formal analysis. **Stefan Wagner:** Conceptualization, Formal analysis, Validation, Writing – original draft. **Astrid Pundt:** Writing – review & editing, Supervision, Resources, Funding acquisition. **Thomas Böhlke:** Writing – review & editing, Supervision, Resources, Funding acquisition.

Declaration of competing interest

The authors declare that they have no known competing financial interests or personal relationships that could have appeared to influence the work reported in this paper.

Acknowledgments

AD and TB gratefully acknowledge partial funding by the Karlsruhe Institute of Technology (KIT), Germany within the EXU funding “KIT Future Fields”, Grant ACDC.

Data availability

The authors are unable or have chosen not to specify which data has been used.

References

Abromeit, A., Siebrecht, R., Song, G., Zabel, H., Klose, F., Nagengast, D., Weidinger, A., 1997. Thickness dependence of the hydrogen solubility in epitaxial Nb (110) films grown on Al2O3 (11.0) substrates. J. Alloys Compd. 253, 58–61.

Adams, B.D., Chen, A., 2011. The role of palladium in a hydrogen economy. Mater. Today 14 (6), 282–289.

Ammar, K., Appolaire, B., Cailletaud, G., Forest, S., 2009. Combining phase field approach and homogenization methods for modelling phase transformation in elastoplastic media. Eur. J. Comput. Mech. 18 (5–6), 485–523.

Anand, L., 2012. A Cahn–Hilliard-type theory for species diffusion coupled with large elastic-plastic deformations. J. Mech. Phys. Solids 60 (12), 1983–2002.

Armand, M., Tarascon, J.-M., 2008. Building better batteries. Nature 451 (7179), 652–657.

Bai, Y., Mianroodi, J.R., Ma, Y., da Silva, A.K., Svendsen, B., Raabe, D., 2022. Chemo-mechanical phase-field modeling of iron oxide reduction with hydrogen. Acta Mater. 231, 117899.

Bair, J., Asle Zaeem, M., Schwen, D., 2017. Formation path of δ hydrides in zirconium by multiphase field modeling. Acta Mater. 123, 235–244.

Baldi, A., Narayan, T.C., Koh, A.L., Dionne, J.A., 2014. In situ detection of hydrogen-induced phase transitions in individual palladium nanocrystals. Nature Mater. 13 (12), 1143–1148.

Barrett, J., Blowey, J., 1999. Finite element approximation of the Cahn–Hilliard equation with concentration dependent mobility. Math. Comp. 68 (226), 487–517.

Burlaka, V., Roddatis, V., Bongers, M.D., Pundt, A., 2017. Defect generation in pd layers by ‘smart’ films with high H-affinity. Sci. Rep. 7 (1), 9564.

Burlaka, V., Wagner, S., Hamm, M., Pundt, A., 2016. Suppression of phase transformation in Nb-H thin films below switchover thickness. Nano Lett. 16 (10), 6207–6212.

Burlaka, V., Wagner, S., Pundt, A., 2015. In-situ STM and XRD studies on Nb–H films: Coherent and incoherent phase transitions. J. Alloys Compd. 645, S388–S391.

Cahn, J.W., Hilliard, J.E., 1958. Free energy of a nonuniform system. I. Interfacial free energy. J. Chem. Phys. 28 (2), 258–267.

Castelli, G.F., von Kolzenberg, L., Horstmann, B., Latz, A., Dörfler, W., 2021. Efficient simulation of chemical–mechanical coupling in battery active particles. Energy Technol. 9 (6), 2000835.

Chen, L., Fan, F., Hong, L., Chen, J., Ji, Y.Z., Zhang, S., Zhu, T., Chen, L., 2014. A phase-field model coupled with large elasto-plastic deformation: application to lithiated silicon electrodes. J. Electrochem. Soc. 161 (11), F3164.

Chester, S.A., Di Leo, C.V., Anand, L., 2015. A finite element implementation of a coupled diffusion-deformation theory for elastomeric gels. Int. J. Solids Struct. 52, 1–18.

Cichy, K., Świerczek, K., 2021. Influence of doping on the transport properties of Y1-xLnxMnO3+ δ (Ln: Pr, Nd). Crystals 11 (5), 510.

Čížek, J., Procházka, I., Kuriplach, J., Danis, I., Kuzel, R., Matěj, Z., Brauer, G., Anwand, W., 2004. Hydrogen-induced defects in bulk Nb. Phys. Rev. B 69 (22), 224106.

Coleman, B.D., Gurtin, M.E., 1967. Thermodynamics with internal state variables. J. Chem. Phys. 47 (2), 597–613.

Copetti, M.I.M., Elliott, C.M., 1992. Numerical analysis of the Cahn–Hilliard equation with a logarithmic free energy. Numer. Math. 63, 39–65.

Di Leo, C.V., Anand, L., 2013. Hydrogen in metals: A coupled theory for species diffusion and large elastic-plastic deformations. Int. J. Plast. 43, 42–69.

Di Leo, C.V., Rejovitzky, E., Anand, L., 2014. A Cahn–Hilliard-type phase-field theory for species diffusion coupled with large elastic deformations: Application to phase-separating Li-ion electrode materials. J. Mech. Phys. Solids 70 (1), 1–29.

Durbin, D.J., Malardier-Jugroot, C., 2013. Review of hydrogen storage techniques for on board vehicle applications. Int. J. Hydrog. Energy 38 (34), 14595–14617.

Dyck, A., Böhlke, T., Pundt, A., Wagner, S., 2024a. Phase transformation in the niobium hydrogen system: Effects of elasto-plastic deformations on phase stability predicted by a thermodynamic model. Scr. Mater. 251, 116209.

Dyck, A., Böhlke, T., Pundt, A., Wagner, S., 2024b. Phase transformation in the palladium hydrogen system: Effects of boundary conditions on phase stabilities. Scr. Mater. 247, 116117.

Dyck, A., Groß, L., Keursten, J., Kehrer, L., Böhlke, T., 2024c. Modeling and FE simulation of coupled water diffusion and viscoelasticity in relaxation tests of polyamide 6. Contin. Mech. Thermodyn. 1–19.

Elliott, C.M., French, D.A., Milner, F., 1989. A second order splitting method for the Cahn–Hilliard equation. Numer. Math. 54, 575–590.

Fernandez, A., Caretta, L., Das, S., Klewe, C., Lou, D., Parsonnet, E., Gao, R., Luo, A., Shafer, P., Martin, L.W., 2021. Strain-induced orbital contributions to oxygen electrocatalysis in transition-metal perovskites. Adv. Energy Mater. 11 (46), 2102175.

Forest, S., Ammar, K., Appolaire, B., 2011. Micromorphic vs. phase-field approaches for gradient viscoplasticity and phase transformations. In: Advances in Extended and Multifield Theories for Continua. Springer, pp. 69–88.

Forest, S., Barbe, F., Cailletaud, G., 2000. Cosserat modelling of size effects in the mechanical behaviour of polycrystals and multi-phase materials. Int. J. Solids Struct. 37 (46–47), 7105–7126.

Fruchter, L., Brouet, V., Colson, D., Moussy, J.-B., Forget, A., Li, Z., 2018. Electrochemical oxygen intercalation into Sr2IrO4. J. Phys. Chem. Solids 112, 1–7.

Fukai, Y., 2005. The Metal-Hydrogen System: Basic Bulk Properties. Springer Series in Materials Science, 21, Springer, Berlin, Heidelberg.

Gear, C.W., 1967. The numerical integration of ordinary differential equations. Math. Comp. 21 (98), 146–156.

Gremaud, R., Gonzalez-Silveira, M., Pivak, Y., De Man, S., Slaman, M., Schreuders, H., Dam, B., Griessen, R., 2009. Hydrogenography of PdHx thin films: Influence of H-induced stress relaxation processes. Acta Mater. 57 (4), 1209–1219.

Griessen, R., Strohfeldt, N., Giessen, H., 2016. Thermodynamics of the hybrid interaction of hydrogen with palladium nanoparticles. Nature Mater. 15 (3), 311–317.

Guo, X., Shi, S.-Q., Zhang, Q., Ma, X., 2008. An elastoplastic phase-field model for the evolution of hydride precipitation in zirconium. Part I: Smooth specimen. J. Nucl. Mater. 378 (1), 110–119.

Gurtin, M.E., Fried, E., Anand, L., 2010. The Mechanics and Thermodynamics of Continua. Cambridge University Press, Cambridge,

Hamm, M., Burlaka, V., Wagner, S., Pundt, A., 2015. Achieving reversibility of ultra-high mechanical stress by hydrogen loading of thin films. Appl. Phys. Lett. 106 (24), 243108.

Han, G., Zhao, Y., Zhou, C., Lin, D.-Y., Zhu, X., Zhang, J., Hu, S., Song, H., 2019. Phase-field modeling of stacking structure formation and transition of δ-hydride precipitates in zirconium. Acta Mater. 165, 528–546.

Heo, T.W., Colas, K.B., Motta, A.T., Chen, L.Q., 2019. A phase-field model for hydride formation in polycrystalline metals: Application to δ-hydride in zirconium alloys. Acta Mater. 181, 262–277.

Jia, Y.-J., Han, W.-Z., 2023. Mechanisms of Hydride Nucleation, Growth, Reorientation, and Embrittlement in Zirconium: A Review. Materials 16 (6), 2419.

Larché, F., Cahn, J.W., 1973. A linear theory of thermochemical equilibrium of solids under stress. Acta Metall. 21 (8), 1051–1063.

Larché, F., Cahn, J.W., 1978. A nonlinear theory of thermochemical equilibrium of solids under stress. Acta Metall. 26 (1), 53–60.

Liu, L.-B., Yi, C., Mi, H.-C., Zhang, S.L., Fu, X.-Z., Luo, J.-L., Liu, S., 2024. Perovskite oxides toward oxygen evolution reaction: Intellectual design strategies, properties and perspectives. Electrochem. Energy Rev. 7 (1), 1–37.

Matsumoto, K., Kawasoko, H., Kasai, H., Nishibori, E., Fukumura, T., 2020. Increased electrical conduction with high hole mobility in anti-ThCr2Si2-type La2O2Bi via oxygen intercalation adjacent to Bi square net. Appl. Phys. Lett. 116 (19), 191901.

McCay, M.H., Shafiee, S., 2020. 22 - Hydrogen: An Energy Carrier. In: Letcher, T.M. (Ed.), Future Energy (Third Edition). Elsevier, pp. 475–493.

Miehe, C., Hildebrand, F.E., Böger, L., 2014. Mixed variational potentials and inherent symmetries of the Cahn–Hilliard theory of diffusive phase separation. Proc. R. Soc. A: Math. Phys. Eng. Sci. 470 (2164), 20130641.

Mises, R.v., 1928. Mechanik der plastischen formänderung von kristallen. ZAMM- J. Appl. Math. Mech./Z. Angew. Math. Mech. 8 (3), 161–185.

Nichols, J., Terzic, J., Bittle, E.G., Korneta, O.B., De Long, L.E., Brill, J., Cao, G., Seo, S.S.A., 2013. Tuning electronic structure via epitaxial strain in Sr2IrO4 thin films. Appl. Phys. Lett. 102 (14), 141908.

Nörthemann, K., Pundt, A., 2008. Coherent-to-semi-coherent transition of precipitates in niobium-hydrogen thin films. Phys. Rev. B 78 (1), 014105.

Nörthemann, K., Pundt, A., 2011. Double-locked nucleation and growth kinetics in Nb-H thin films. Phys. Rev. B Condens. Matter Mater. Phys. 83 (15), 1–10.

Phan, A.T., Gheribi, A.E., Chartrand, P., 2019. Modeling of coherent phase transformation and particle size effect in LiFePO4 cathode material and application to the charging/discharging process. Electrochim. Acta 295, 632–644.

Pivak, Y., Schreuders, H., Slaman, M., Griessen, R., Dam, B., 2011. Thermodynamics, stress release and hysteresis behavior in highly adhesive Pd–H films. Int. J. Hydrog. Energy 36 (6), 4056–4067.

Prahs, A., Schöller, L., Schwab, F.K., Schneider, D., Böhlke, T., Nestler, B., 2023. A multiphase-field approach to small strain crystal plasticity accounting for balance equations on singular surfaces. Comput. Mech. 1–22.

Rahm, J.M., Löfgren, J., Erhart, P., 2022. Quantitative predictions of thermodynamic hysteresis: Temperature-dependent character of the phase transition in Pd–H. Acta Mater. 227, 117697.

Schneemann, A., White, J.L., Kang, S., Jeong, S., Wan, L.F., Cho, E.S., Heo, T.W., Prendergast, D., Urban, J.J., Wood, B.C., et al., 2018. Nanostructured metal hydrides for hydrogen storage. Chem. Rev. 118 (22), 10775–10839.

Schober, T., Wenzl, H., 1978. Hydrogen in metals II. Top. Appl. Phys. 29, 11–71.

Schwarz, R., Khachaturyan, A., 1995. Thermodynamics of open two-phase systems with coherent interfaces. Phys. Rev. Lett. 74 (13), 2523.

Schwarz, R., Khachaturyan, A., 2006. Thermodynamics of open two-phase systems with coherent interfaces: Application to metal–hydrogen systems. Acta Mater. 54 (2), 313–323.

Schwarz, R., Khachaturyan, A., Caro, A., Baskes, M., Martinez, E., 2020. Coherent phase decomposition in the Pd–H system. J. Mater. Sci. 55 (11), 4864–4882.

Schwarze, C., Gupta, A., Hickel, T., Kamachali, R.D., 2017. Phase-field study of ripening and rearrangement of precipitates under chemomechanical coupling. Phys. Rev. B 95 (17), 174101.

Shi, S., Markmann, J., Weissmüller, J., 2018. Verifying Larché–Cahn elasticity, a milestone of 20th-century thermodynamics. Proc. Natl. Acad. Sci. 115 (43), 10914–10919.

Simo, J.C., Hughes, T.J.R., 1998. Computational Inelasticity. Interdisciplinary Applied Mathematics, 7, Springer-Verlag, New York.

Simon, P.C., Aagesen, L.K., Jokisaari, A.M., Chen, L.Q., Daymond, M.R., Motta, A.T., Tonks, M.R., 2021. Investigation of δ zirconium hydride morphology in a single crystal using quantitative phase field simulations supported by experiments. J. Nucl. Mater. 557, 153303.

Smith, M., 2009. ABAQUS/Standard User's Manual, Version 6.9. Dassault Systèmes Simulia Corp, United States.

Sofronis, P., McMeeking, R.M., 1989. Numerical analysis of hydrogen transport near a blunting crack tip. J. Mech. Phys. Solids 37 (3), 317–350.

Song, G., Remhof, A., Labergerie, D., Zabel, H., 2002. Kinetics of hydrogen absorption and desorption in epitaxial thin niobium films. Phys. Rev. B 66 (4), 045407.

Spatschek, R., Gobbi, G., Hüter, C., Chakrabarty, A., Aydin, U., Brinckmann, S., Neugebauer, J., 2016. Scale bridging description of coherent phase equilibria in the presence of surfaces and interfaces. Phys. Rev. B 94 (13), 134106. Steinbach, I., 2009. Phase-field models in materials science. Modelling Simul. Mater. Sci. Eng. 17 (7), 073001.

Steinbach, I., Shchyglo, O., 2011. Phase-field modelling of microstructure evolution in solids: Perspectives and challenges. Curr. Opin. Solid State Mater. Sci. 15 (3), 87–92.

Switendick, A., 1979. Band structure calculations for metal hydrogen systems. Z. Phys. Chem. 117 (117), 89–112.

Ubachs, R.L., Schreurs, P.J., Geers, M.G., 2004. A nonlocal diffuse interface model for microstructure evolution of tin-lead solder. J. Mech. Phys. Solids 52 (8), 1763–1792.

Voskuilen, T.G., Pourpoint, T.L., 2013. Phase field modeling of hydrogen transport and reaction in metal hydrides. Int. J. Hydrog. Energy 38 (18), 7363–7375.

Wagner, S., Klose, P., Burlaka, V., Nörthemann, K., Hamm, M., Pundt, A., 2019. Structural phase transitions in niobium hydrogen thin films: Mechanical stress, phase equilibria and critical temperatures. ChemPhysChem 20 (14), 1890–1904.

Wagner, S., Pundt, A., 2016. Quasi-thermodynamic model on hydride formation in palladium–hydrogen thin films: Impact of elastic and microstructural constraints. Int. J. Hydrog. Energy 41 (4), 2727–2738.

Wagner, S., Uchida, H., Burlaka, V., Vlach, M., Vlcek, M., Lukac, F., Cizek, J., Baehtz, C., Bell, A., Pundt, A., 2011. Achieving coherent phase transition in palladium-hydrogen thin films. Scr. Mater. 64 (10), 978–981.

Weissmüller, J., 2024. Coherent phase change in interstitial solutions: A hierarchy of instabilities. Adv. Sci. 2308554.

Wicht, D., Schneider, M., Böhlke, T., 2020. An efficient solution scheme for small-strain crystal-elasto-viscoplasticity in a dual framework. Comput. Methods Appl. Mech. Engrg. 358, 112611.

Wicke, E., Brodowsky, H., Züchner, H., 2005. Hydrogen in palladium and palladium alloys. In: Hydrogen in Metals II: Application-Oriented Properties. Springer, pp. 73–155.

Wodo, O., Ganapathysubramanian, B., 2011. Computationally efficient solution to the Cahn–Hilliard equation: Adaptive implicit time schemes, mesh sensitivity analysis and the 3D isoperimetric problem. J. Comput. Phys. 230 (15), 6037–6060.

Xia, J., Zhang, N., Yang, Y., Chen, X., Wang, X., Pan, F., Yao, J., 2023. Lanthanide contraction builds better high-voltage LiCoO2 batteries. Adv. Funct. Mater. 33 (8), 2212869.

Zabel, H., Peisl, H., 1979. Sample-shape-dependent phase transition of hydrogen in niobium. Phys. Rev. Lett. 42 (8), 511.

Zhang, L., Tonks, M.R., Gaston, D., Peterson, J.W., Andrs, D., Millett, P.C., Biner, B.S., 2013. A quantitative comparison between C0 and C1 elements for solving the Cahn–Hilliard equation. J. Comput. Phys. 236, 74–80.

Zhu, Y., Wook Heo, T., Rodriguez, J.N., Weber, P.K., Shi, R., Baer, B.J., Morgado, F.F., Antonov, S., Kweon, K.E., Watkins, E.B., Savage, D.J., Chapman, J.E., Keilbart, N.D., Song, Y., Zhen, Q., Gault, B., Vogel, S.C., Sen-Britain, S.T., Shalloo, M.G., Orme, C., Bagge-Hansen, M., Hahn, C., Pham, T.A., Macdonald, D.D., Roger Qiu, S., Wood, B.C., 2022. Hydriding of titanium: Recent trends and perspectives in advanced characterization and multiscale modeling. Curr. Opin. Solid State Mater. Sci. 26 (6), 101020.

Züttel, A., Borgschulte, A., Schlapbach, L. (Eds.), 2008. Hydrogen as a Future Energy Carrier, 1 Wiley, Berlin.